A MISO Frequency Diverse Array Implementation

Nicholas Kellerman

Submitted to the graduate degree program in Department of Electrical Engineering and Computer Science and the Graduate Faculty of the University of Kansas in partial fulfillment of the requirements for the degree of Master's.

Committee members

Patrick McCormick, Chairperson

Shannon Blunt, Committee Member

Christopher Allen, Committee Member

James Stiles, Committee Member

Date defended: May 10th, 2023

This work was supported by the US Air Force Research Lab under Contract #FA8650-18-3-9326.
DISTRIBUTION STATEMENT A. Approved for public release.

The Thesis Committee for Nicholas Kellerman certifies
that this is the approved version of the following thesis:

A MISO Frequency Diverse Array Implementation

Patrick McCormick, Chairperson

Date approved: May 11th, 2023

Abstract

The separation of RF signals from different angles of arrival is a key objective for a radar receiver. A common approach to spatial separation relies on the measurement of a linear phase progression across multiple receive antenna elements, where the rate of progression relates directly to a spatial angle of arrival.

With a single antenna receiver, spatial separation can still be achieved using spatially diverse emission structures. One such emission structure is the Frequency Diverse Array (FDA), which transmits a frequency shifted version of a common waveform out of each element. Due to the frequency shifts, the peak of the mainbeam sweeps across time and space.

With a careful choice of waveform and frequency shift, the waveforms transmitted from each element can be identified and separated in delay, and only a single receiver antenna element is needed to measure a phase progression across the waveform responses or "virtual array" in delay.

In this thesis, a Multiple Input Single Output (MISO) radar system capable of performing range, Doppler, and spatial estimation will be presented and experimentally validated. The system leverages key features of the LFMCW-FDA emission structure to achieve a single channel receiver architecture which can realize the aforementioned performance and simultaneously remain computationally inexpensive. When compared to other spatially diverse emissions, the system is shown to retain the unambiguous range and Doppler spaces. The potential for this type of emission structure to be used in a search radar context is also explored. Additionally, an adaptive processing algorithm will be introduced along with simulated results showing an improved ability to separate closely spaced scatterers in range and space.

Acknowledgements

First, I can't thank either Dr. Blunt or Dr. McCormick enough for their teaching, guidance, and patience with me throughout my graduate studies. Having the opportunity to learn and work alongside them as well as the incredibly talented cast around the research lab is an experience I will forever be grateful for. Second, I'd like to thank Dr. Stiles and Dr. Allen for not only agreeing to being members of my thesis committee, but also for the openness and ease with which they freely share with students all the invaluable knowledge they've gained over their careers. Third, to David Felton and Andrew Mertz, thank you both for sharing awesome summers with me in D.C. and Dayton, respectively. Last but not least, to all my friends, my family, and my dog Kat, from the bottom of my heart, thank you.

Contents

List of Figures

List of Tables

Chapter 1

Introduction

1.1 Motivation

The theory, analysis and results presented within this report were generated in support of a project which aimed to demonstrate a radar system framework which could

1. Accomplish the goals of a search radar (efficient illumination and estimation of scattering over a large area of space)

2. Maintain a low cost receiver architecture

To achieve this aim, a Multiple Input Single Output (MISO) system was designed, which leverages the attributes of a Linear Frequency Modulated Continuous Wave Frequency Diverse Array (LFMCW-FDA) transmission to accomplish spatial, range, and Doppler processing using a single receive antenna element.

This MISO LFMCW-FDA implementation can be thought of effectively as the inverse of the Ubiquitous radar concept [1], where instead of widebeam on transmit, a widebeam on receive, and separability of the waveforms allows the ability to distinguish distinct scattering received from different spatial locations.

The work presented in the following sections will detail theory, explore simulated results, and demonstrate experimental validation of such a radar system. The system will be compared to other spatially diverse emission structures. It will likewise be shown to have attractive features for use as a low resolution search radar. Improvement in the separability of closely spaced scatterers in range and spatial angle via an adaptive algorithm will also be introduced with simulated results

supporting its use.

The remainder of this section introduces the basic radar concepts which are fundamental to the theory of the LFMCW-FDA MISO system and receive processing.

1.2 Radar Fundamentals

Active radar systems can be classified as either CW or pulsed systems. A CW radar is one in which the transmit antenna is always radiating, and the receive antenna is always receiving. In contrast, a pulsed radar emits higher power energy (relative to the CW case) in short intervals, or pulses, and then immediately after there is a receive time interval where the transmitter is not radiating.

The basic goal of any radar system is to estimate the scattering parameters of the reflecting objects in a scene. Important parameters include the object's distance or range away from the platform, the speed of the object, and the spatial angle of the object relative to the "look" direction of the radar. This spatial angle can extend to two dimensions - the horizontal axis, often called the azimuth angle, and the vertical axis, the elevation angle. Together, these parameters can provide an estimate of an object's size and/or physical makeup, location, and bearing out in space.

1.2.1 Range Estimation & Pulse Compression

The simplest and most fundamental radar operation is that of determining the range of objects in a scene. Consider the simple pulsed radar example. An antenna transmits a rectangular pulse of time duration T - the pulse travels a distance R_1 at the speed of light c - the pulse hits an object which scatters or reflects RF energy - and a portion of the RF energy returns back to the same antenna which now receives the reflection.

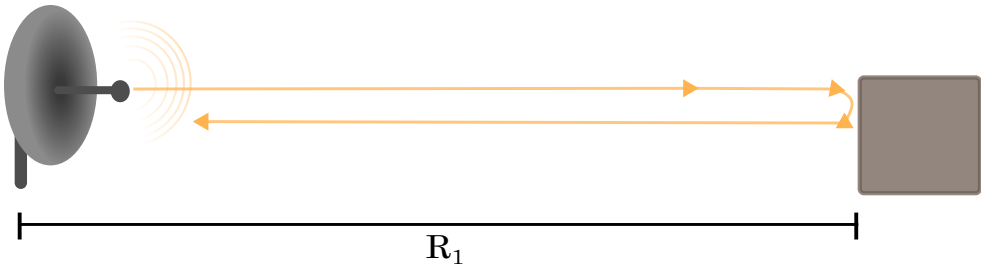

Figure 1.1: Simple 1D Range Example

An example of what both the transmit pulse of length T and receive signal for time delay might look like for a scatterer at delay τ_1 is shown below:

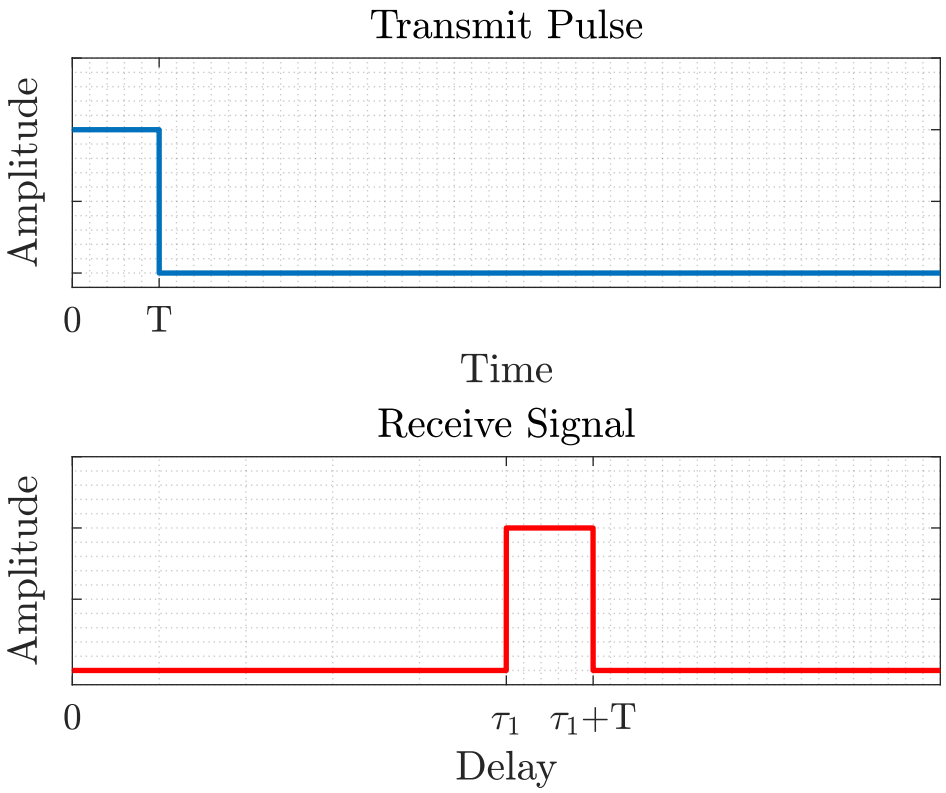

Figure 1.2: Amplitude vs Time/Delay Example

The amount of time it takes for the RF energy to be emitted, reflect off the scatterer, and return to the receiver is the delay τ, and has the following relationship with the range R_1 of the scatterer:

$$\tau_1 = \frac{2R_1}{c} \tag{1.1}$$

Equation 1.1 is the two-way time delay for the scatterer a distance R_1 away from the radar platform. By measuring τ_1, one can likewise estimate the scattering's distance or range.

Measuring the time delay of a received signal isn't the only way a range measurement can be established. In fact, it is not an attractive means of doing so, in large part due to the issue of poor range resolution, or the ability to discern between two closely spaced scatterers. To demonstrate this issue, reconsider the setup from above in Figure 1.1. Now add a second scatterer, located at a range R_2. With this scenario depicted in Figure 1.3, consider 2 possible resulting receive signals in Figure 1.4, which depend on how closely spaced the scatterers are relative to each other, represented as Δx:

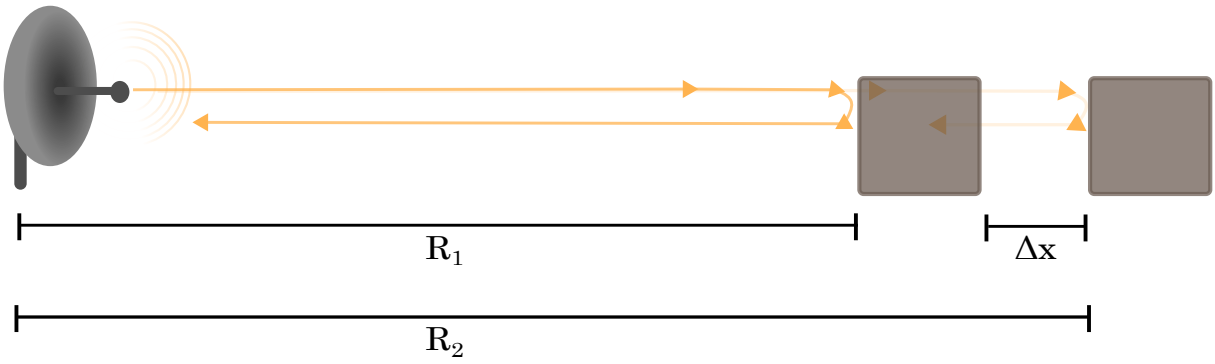

Figure 1.3: Amplitude vs Delay, Multiple Scatterers

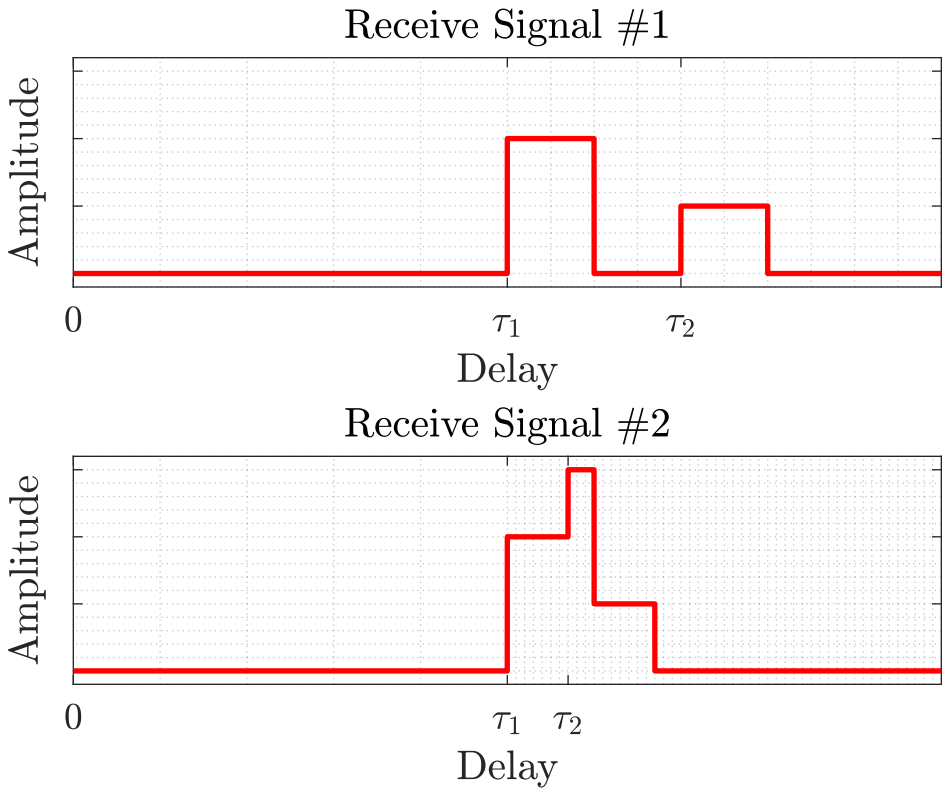

Figure 1.4: Simple 1D Range Example, Multiple Scatterers

In Figure 1.4, the top plot shows the response for two scatterers spaced adequately apart - it can be clearly seen that two separate scatterers are present. The bottom plot shows two scatterers placed too close together - no longer can the two scatterers be resolved; there appears to be only a single, extended scatterer. Depending on the distance Δx between the two scatterers, their resulting responses might interfere with one another, which makes determining whether there is one or more scatterers difficult.

In this simple case of the rectangular pulse, the ability to distinguish between two scatterers is determined by the length of the pulse T. When scatterers are separated by a range corresponding to the two-way time delay of T, two separate responses can be seen, and thus ranges can be estimated for both. This determines the range resolution ΔR, and can be expressed by rearranging the previous delay equation, and plugging in ΔR and T:

$$\Delta R = \frac{cT}{2} \tag{1.2}$$

In general an active pulsed radar system is designed for longer pulses, to achieve more energy on target. However, longer pulses results in a poor ΔR. This directly motivates the need for a technique to improve the ability to resolve closely spaced scatterers, like pulse compression.

Pulse compression is a technique which utilizes Frequency Modulated (FM) waveforms of bandwidth B on transmit and a correlation procedure on receive to generate a range estimate. A classic example of pulse compression involves transmitting a Linear Frequency Modulated (LFM) waveform, or chirp. This technique results in a superior range resolution, which can be expressed as:

$$\Delta R = \frac{c}{2B} \tag{1.3}$$

In short terms, the pulse compression response effectively shortens, or compresses, the response of a scatterer in delay, hence the name. Intuitively, if the response of a scatterer is shortened in delay, then it makes sense that the ability to distinguish between closely spaced scatterers is improved. This transmission and filtering procedure can also be referred to as delay and/or range compression.

The Pulse Repetition Interval (PRI) is the full time interval of transmit and receive before the proceeding pulse is emitted. The PRI or T_{PRI} sets the maximum possible unambiguous range R_{ua} as

$$R_{ua} = \frac{cT_{PRI}}{2} \tag{1.4}$$

1.2.2 Doppler Processing

Another fundamental parameter radar systems are tasked with determining is how quickly a scatterer is moving towards or away from the radar platform. Traditionally, this is done by observation

of the Doppler effect on a received signal.

Consider the case where a scatterer is moving at a constant radial velocity v_r. When a transmitted signal of center frequency $f_c = \frac{c}{\lambda_c}$ hits this scatterer moving radially towards or away from the radar platform, a Doppler frequency shift f_d is imparted to the signal. The frequency shift is proportional to the radial velocity of the moving scatterer and the center wavelength λ_c as

$$f_d = \frac{2v_r}{\lambda_c} \tag{1.5}$$

The maximum observable Doppler shift is determined by the Pulse Repetition Frequency (PRF) of the radar, which is the inverse of the PRI. Any shifts larger in magnitude than the max Doppler shift will alias back into the observable Doppler space and thus an ambiguous Doppler shift will appear. The maximum unambiguous Doppler shift f_{ua} is defined as

$$f_{ua} = \frac{PRF}{2} \tag{1.6}$$

In most scenarios, many pulses are required to achieve a sufficient observation time of the scene in order to have the ability to resolve Doppler frequency shifts in scattering responses. The time over which a sufficient number of pulses can be collected which satisfies this requirement is referred to as a Coherent Processing Interval (CPI), and will also be denoted at times as T_{CPI} or integration time within this work.

By collecting a CPI's worth of pulses, Doppler shifts can be estimated by taking a Fourier Transform at every delay bin across pulses. The Doppler resolution Δf_d is related to the integration time as

$$\Delta f_d = \frac{1}{T_{CPI}} \tag{1.7}$$

1.2.3 The Uniform Linear Array and Spatial Estimation

The well known Uniform Linear Array (ULA) is the assumed transmit antenna array structure considered throughout the remainder of this work, and so will be defined here. The ULA is composed of a collection of individual antenna elements arrayed along a single Cartesian dimension, with the following properties:

- The array is comprised of M antenna elements
- Each element is identical and radiates isotropically (no directional gain)
- Each element emits RF energy at a center frequency f_c, where wavelength $\lambda_c = \frac{c}{f_c}$ for speed of light c
- The elements are spaced a uniform distance $d = \frac{\lambda_c}{2}$ apart from each other
- The time required for a signal to travel across the array is significantly smaller than the inverse of the bandwidth of the signal (narrowband assumption)

An important assumption in this discussion of spatial estimation is that signals impinging on the face of the ULA are in the far-field. Thus the incident signal is assumed to be a plane wave, where the phase fronts wash over the array in a linear fashion.

The ULA with incident phase fronts can be visualized with the following figure:

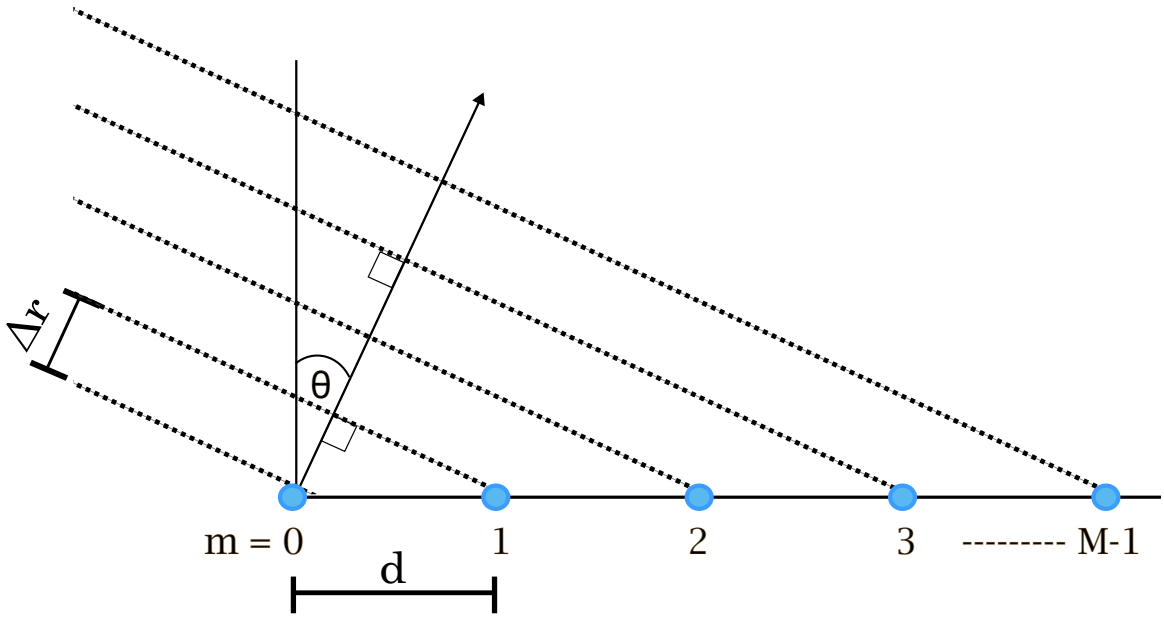

Figure 1.5: Uniform Linear Array and Impinging Phase Fronts

For the ULA, spatial angle θ is referenced to the boresight angle, which is the axis of symmetry of the array.

Note that individual elements are referenced with the script m, and that the reference indexing begins with the reference element $m = 0$ (which is also called the "phase center") and continues til the index $M - 1$. This convention is arbitrary - a different indexing could be chosen - all that matters is that this convention is adhered to, and so this is the convention used in the rest of this work, unless specifically stated otherwise.

To begin the discussion on spatial estimation, consider a plane wave incident on the face of the ULA at angle θ_o. The physical distance between the phase front from one element to the next is Δr, found using Figure 1.5 and trigonometry:

$$\Delta r = \cos(\theta_o - 90)d = \sin(\theta_o)d$$

The phase progression associated with this physical distance can be found by multiplying Δr by the spatial frequency or wavenumber $k = \frac{2\pi}{\lambda_c}$. Due to the uniformity of the spacing of the elements,

the phase progression for the m^{th} element referenced to the phase center is simply

$$m \cdot k \cdot \Delta r = m \frac{2\pi}{\lambda_c} \sin(\theta_o) d$$

The signal $y_m(t)$ received at the m^{th} element can be expressed in terms of the signal $s(t)$ received at the reference, along with added phase rotation to account for the physical distance away from the phase center as:

$$y_m(t) = s(t) e^{j \frac{2\pi}{\lambda_c} d \sin(\theta_o) m}$$

Conceptually, the received signal $y_m(t)$ can be thought of as the signal $s(t)$ offset in spatial frequency by $\sin(\theta)$, where the element index m is to spatial frequency what time t is to temporal frequency f. With this in mind, the M spatial samples contain the same spatial frequency offset, for different values of m. And just as the temporal frequency content of a signal can be revealed through the Fourier transform of the signal, so can the spatial frequency content, via a similar process, where instead of a transformation from time to frequency, it is a transformation from element-space to spatial frequency. The form looks very similar to that of a Discrete Fourier Transform. This transformation is also referred to as "standard beamforming", and the resulting beamformed response $Y(t, \theta)$ can be expressed mathematically as follows:

$$\begin{aligned} Y(t, \theta) &= \sum_{m=0}^{M-1} y_m(t) e^{-j \frac{2\pi}{\lambda_c} d \sin(\theta) m} \\ Y(t, \theta) &= \sum_{m=0}^{M-1} s(t) e^{j \frac{2\pi}{\lambda_c} d \sin(\theta_o) m} e^{-j \frac{2\pi}{\lambda_c} d \sin(\theta) m} \end{aligned} \tag{1.8}$$

From observation, the peak value of $Y(t, \theta)$ will occur when $\theta = \theta_o$. Thus, an estimate of the incident angle θ_o can be achieved by beamforming across all possible spatial angles.

Recalling the Fourier transform of a rectangular pulse, a sinc function results with a peak to null relationship dependent on the length of the pulse in time. As the rectangular pulse lengthens,

the peak to null length decreases, sharpening the response. Similarly, the ULA can be thought of as a rectangular function in space, and with more elements in the ULA, the sharper the spatial frequency response, which dictates the spatial resolution $\Delta\theta$. From [2], the spatial resolution for an array of length L and center frequency λ_c is approximated as (in radians):

$$\Delta\theta \approx \frac{\lambda_c}{L} \tag{1.9}$$

For the ULA case, L can be expressed in terms of the number of elements M and element spacing d as

$$L = (M-1)d$$

Plugging this into (1.9)

$$\Delta\theta \approx \frac{\lambda_c}{(M-1)d} \tag{1.10}$$

It is important to note that the same physical relationships hold for a ULA transmitting a signal $s(t)$ centered at f_c, meaning the transmitted signal $s_m(t)$ from the m^{th} element can be focused to spatial direction θ_0' by applying the necessary phase rotation to each element on transmit:

$$s_m(t) = s(t)e^{j\frac{2\pi}{\lambda_c}d\sin(\theta_o')m}$$

1.3 Radar Waveforms

In the previous sections, the pulsed radar case with pulsed radar waveforms was considered, primarily for convenience in introducing range and Doppler processing. The remainder of the work deals with CW waveforms. The previous results for range and Doppler performance are still applicable, with one minor alteration. In CW, there is technically no PRI or PRF; however, since the transmitted waveform repeats in CW, the waveform repetition interval T is now the effective PRI,

with the effective PRF being $\frac{1}{T}$.

Proper choice of the transmit waveform depends on the objectives of the radar system and the expected environment in which the system will operate, among many other practical considerations. Multiple-Input Multiple-Output or MIMO waveforms take advantage of radar systems capable of both transmitting and receiving on independent channels. This capability is often viewed in contrast to the phased array radar, wherein the same waveform is emitted from each element of an array with an added element-wise phase progression for beamforming purposes, as previously discussed.

There are two general classes of MIMO radars: Separated MIMO, where transmit and receive antennas are separated by considerable distances and the signals received by array elements are uncorrelated, and colocated MIMO, where the transmit and receive antennas are either the same physical elements or are spaced closely enough that the incidence angle is treated as the same for either transmit or receive array, and the received signal by array elements are highly correlated. For the purposes of this work, the colocated case is assumed when referring to MIMO from here on. For further description and context of colocated MIMO, see [3].

MIMO radar waveforms that can be distinctly differentiated from one another in a given domain (time, Doppler, delay) are often referred to as spatially diverse emission structures. Two well known spatially diverse MIMO structures are Doppler Division Multiple Access (DDMA) [4], [5] and Time Division Multiple Acess (TDMA) [6].

1.3.1 Doppler Division Multiple Access

In DDMA, an element-wise frequency offset ΔF is added to each transmit waveform $s(t)$, where the waveform $s_m(t)$ emitted from the m^{th} element can be expressed as:

$$s_m(t) = s(t)e^{j2\pi\Delta F t m} \tag{1.11}$$

As will be shown in the next section, this expression is identical to the FDA. The key difference

between FDA and DDMA is in the choice of ΔF. In DDMA, this frequency offset is chosen such that each waveform is effectively Doppler shifted by a uniform fraction of the unambiguous Doppler space. For M FMCW waveforms, the unambiguous Doppler space is partitioned as $\frac{1}{MT}$. Rewriting (1.11):

$$s_m(t) = s(t)e^{j2\pi\frac{m}{MT}t} \tag{1.12}$$

Each $s_m(t)$ is distinguishable by the associated $\frac{m}{MT}$ frequency shift, resulting in the ability to separate individual waveforms in the Doppler domain. An example DDMA response for a scatterer at zero delay and zero Doppler shift:

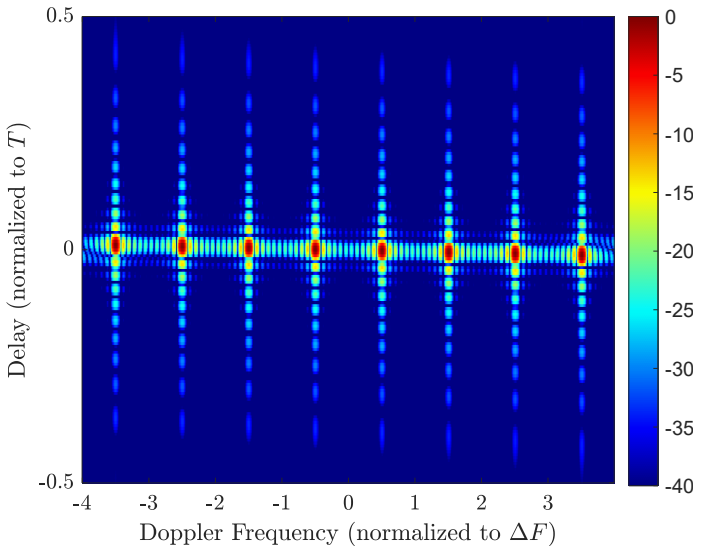

Figure 1.6: Example DDMA response, for $M = 8$ transmit antenna elements, LFMCW waveform

Note that in Figure 1.6, responses are offset from integer multiples of ΔF, and this is to avoid a response occurring at zero Doppler, within the clutter region. Thus the choice of element indexing is critical here. For an integer multiple indexing (such as 0:M-1), the element-wise frequency offsets f_m would need to be altered slightly as:

$$f_m = \left(m - \frac{(M-1)}{2}\right)\Delta F \tag{1.13}$$

A key drawback to this emission is the reduction in the unambiguous velocity space. The new unambiguous velocity $f_{d_{ua}}$ is now equivalent to frequency offset ΔF:

$$f_{d_{ua}} = \Delta F = \frac{1}{MT} \tag{1.14}$$

1.3.2 Time Division Multiple Access

In TDMA, the waveform $s(t)$ of duration T is transmitted individually by each element in a non-overlapping sequence. A variant of this TDMA structure will be considered here, shown experimentally in [6], where each element begins to transmit the waveform at staggered, overlapping time intervals specified by a delay ΔT. This can be expressed as:

$$s_m(t) = s(t - m\Delta T) \tag{1.15}$$

After pulse compression, waveform separability is achieved in the delay domain. An example response for a scatterer at zero delay and zero Doppler:

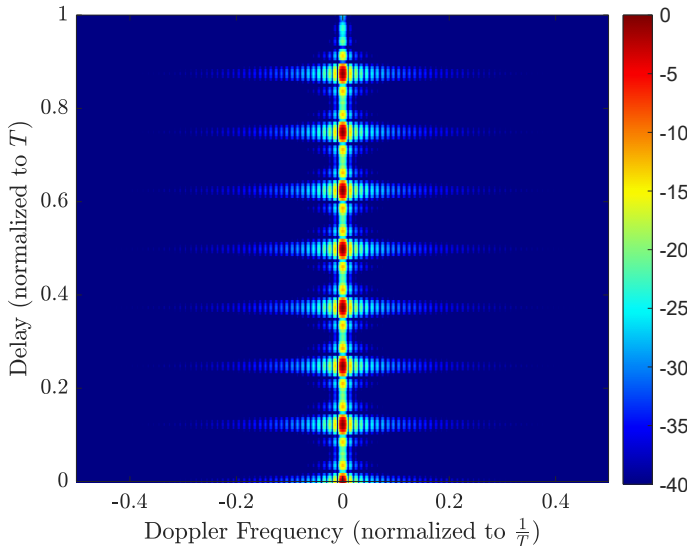

Figure 1.7: Example TDMA for $M = 8$ transmit antenna elements, LFMCW waveform

A key drawback here is a reduction in the unambiguous range R_{ua}, which is now reduced by

the time delay offsets $\frac{T}{M}$

$$R_{ua} = \frac{cT}{2M} \tag{1.16}$$

A third MIMO emission structure, which will be presented in detail in the next section, is the Frequency Diverse Array (FDA). The first published discussion on the FDA concept was by Antonik [7]. At a high level, the FDA applies an element-wise frequency offset to the waveform emitted from each element of an array. As a result of this FDA structure, the peak of the mainbeam "sweeps" across the spatial dimension over the transmission time interval. This sweeping nature and more will be discussed in detail in the next section.

1.4 Search Radar

Traditional radar systems involved in search and track are pulsed systems that employ a scanning pattern for search. A traditional search scan pattern involves the formation and steering of a pencil beam across a desired spatial extent, where steering is accomplished either mechanically via rotating platform, or electronically via phase shifting.

After detection, a systemized way of updating target tracks is required. Two such methods considered in this analysis are Track-while-Scan (TWS) and Search-and-Track (SAT). The TWS method does not alter the scan pattern to accommodate updates on target positions; target tracks are updated at a constant scan rate across all spatial angles.

Conversely, the SAT method prioritizes certain spatial angles over others when detected targets of interest are present, diverting resources away from the scan in order to fixate on a particular direction. As a consequence, the update rate for other spatial angles suffers.

In comparison, the TWS method is best used in contexts where a constant update rate is acceptable. The SAT method is better suited for contexts where a priority based on perceived threat will occur at some spatial angles relative to others.

While detection and tracking are not explored in this work, in the following section the LFMCW-

FDA emission will be assessed in the context of a search radar, and revealed as an attractive emission structure which provides a constant revisit rate similar to that of TWS while also maintaining the ability to vary the revisit rate similar to SAT.

Chapter 2

LFMCW-FDA Emission

This section introduces the transmission structure which will be used in the system under consideration. It will be shown that the combination of LFMCW waveforms and a FDA structure results in a time-varying beampattern that sweeps the main beam across spatial angles over the chirp time. This accomplishes persistent illumination of the radar scene without the need for mechanical scanning or electronic scanning with phase shifters, an attractive feature for a search radar.

The FDA concept was formally introduced by Antonik in [7], and has been thoroughly investigated [8] [9]. The combination of FDA and LFM waveforms was explored in a follow-up paper [10] by Antonik, addressing the possibilities of this combination for use in Moving Target Indication (MTI) and Synthetic Aperature Radar (SAR) contexts.

A planar FDA concept has also been explored in [11], where the beam scanning nature extends to both azimuth and elevation angles across time, increasing the spatial diversity. Although only the 1-D ULA case is explored in this work, the planar array geometry and associated spatial diversity is an attractive topic for future exploration and potential extension of this work.

2.1 The Frequency Diverse Array (FDA)

Given a ULA of M elements spaced a distance $d = \frac{\lambda_c}{2}$ apart, with center frequency f_c, and emitting a waveform $s(t)$ of duration T, a FDA introduces an element-wise frequency offset ΔF to the waveform emitted by the m^{th} antenna element $s_m(t)$, which can be written as:

$$s_m(t) = s(t)e^{j2\pi\Delta Ftm} \tag{2.1}$$

The complex far-field radiated emission pattern $g(t,\theta)$ describes the constructive/destructive interference of the total emission, across time t and space θ. This can be expressed as the superposition of the waveforms $s_m(t)$, along with the element-wise phase rotation associated with any given spatial direction θ, and an added element-wise phase offset ϕ_o:

$$\begin{aligned} g(t,\theta) &= \frac{1}{M}\sum_{m=0}^{M-1} s_m(t)e^{j\pi\sin(\theta)m} \\ &= \frac{1}{M}\sum_{m=0}^{M-1} s(t)e^{j[2\pi\Delta Ft+\pi\sin(\theta)+\phi_o]m} \end{aligned} \tag{2.2}$$

Where the division by M is used to normalize the expression to unity gain. Looking at the element-wise phase function of the complex exponential in 2.2, the expression is dependent on both time and space:

$$\phi_m(t,\theta) = [2\pi\Delta Ft + \pi\sin(\theta) + \phi_o]\, m \tag{2.3}$$

Thus, the FDA structure couples the space and time dimensions. A direct consequence of this is the location of the coherent mainbeam of this emission. The peak of the mainbeam can be found where the value of the phase function is equal to integer multiples of 2π, including zero:

$$\phi_m(t,\theta) = 2\pi\cdot k \tag{2.4}$$

$$k = 0,1,...$$

Considering the consequence of (2.4), two things become clear when observing (2.3). First, owing to the term involving frequency offset ΔF, the location of the peak is now a linear function of time. Secondly, constant ϕ_o controls the spatial angle where the peak begins at time $t = 0$.

2.2 MISO LFMCW-FDA Emission Structure

The waveform $s(t)$ chosen for this system is an up-chirping FMCW waveform of bandwidth B and chirp duration T which sweeps from $\frac{-B}{2}$ to $\frac{B}{2}$, and for N chirps can be expressed as:

$$s(t) = \sum_{n=0}^{N-1} u(t - nT) \tag{2.5}$$

Where

$$u(t) = e^{j2\pi(\frac{B}{2T}t^2 - \frac{B}{2}t)}$$

$$0 \leq t \leq T$$

The instantaneous frequency function $f(t)$ is the time derivative of the phase function $\theta(t)$ for the LFM:

$$f(t) = \frac{d\theta(t)}{dt}\frac{1}{2\pi} = \frac{B}{T}t - \frac{B}{2} \tag{2.6}$$

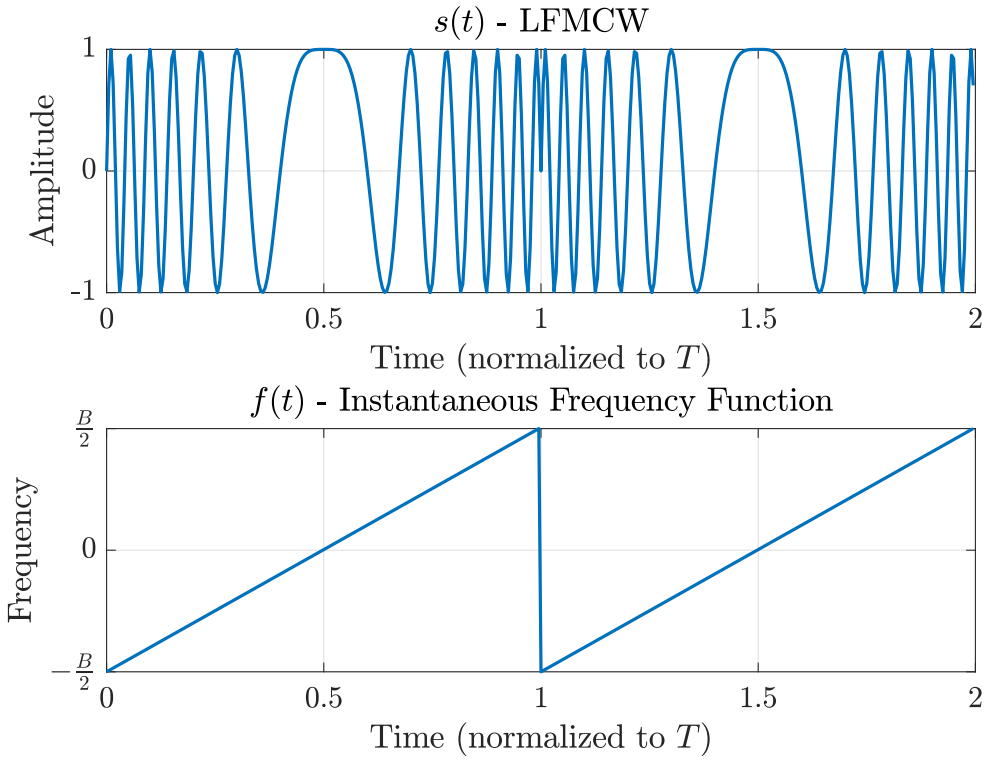

Figure 2.1: s(t) and f(t)

Combining the LFMCW waveform of (2.5) with the FDA structure of (2.2), and choosing $\Delta F = 1/T$, $\phi_o = -\pi$ yields the LFMCW-FDA emission structure:

$$g(t,\theta) = \frac{1}{M}\sum_{m=0}^{M-1}\sum_{n=0}^{N-1} e^{j2\pi\left(\frac{B}{2T}(t-nT)^2-\frac{B}{2}(t-nT)\right)} e^{j\left(2\pi\frac{t}{T}+\pi\sin(\theta)-\pi\right)m} \tag{2.7}$$

The choice of ΔF ensures a full spatial sweep is equivalent to a full frequency sweep, and ϕ_o was chosen to ensure that the mainbeam peaks at $\theta = 0^\circ$ half-way through the sweep ($t = \frac{T}{2}$). This results in the Time-Varying Beam Pattern (TVBP) expressed as $|g(t,\theta)|^2$ (for $N = 1$ sweep and $\sin\theta$):

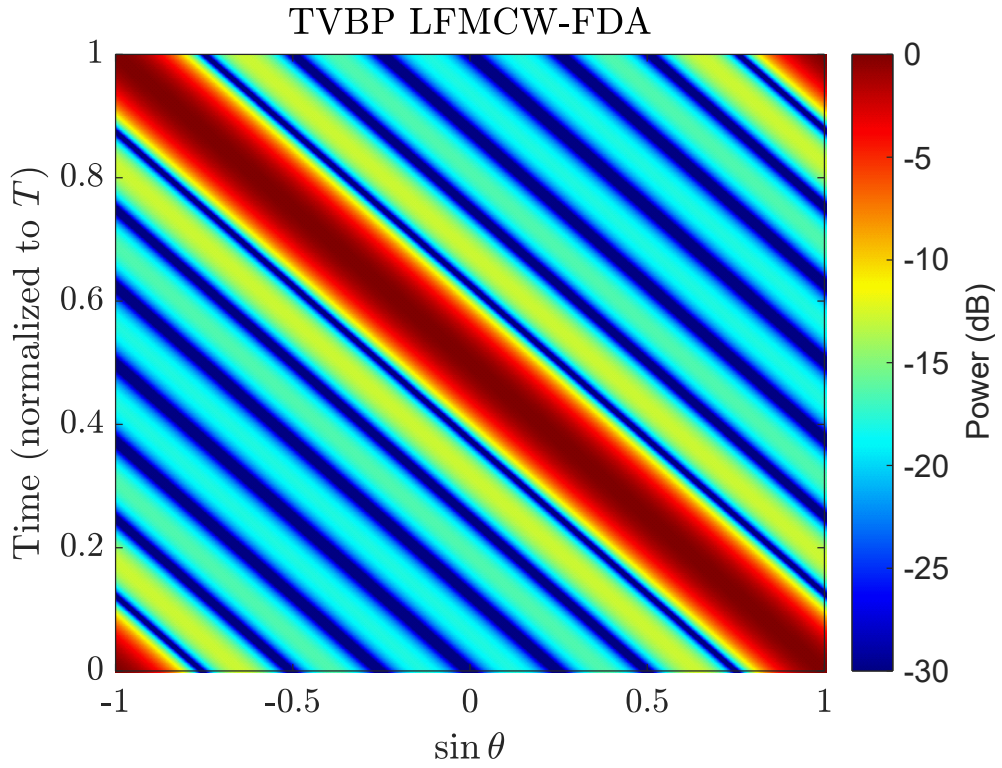

Figure 2.2: TVBP for the LFMCW-FDA emission, single sweep, $\phi_o = -\pi$, $\Delta F = 1/T$,$M = 8$

The FDA couples space and time and the LFM waveform couples time and frequency. The combination of the two results in a space-frequency coupling, which can be visualized by taking the Fourier transform of $g(t,\theta)$ which results in a spatially varying energy spectral density.

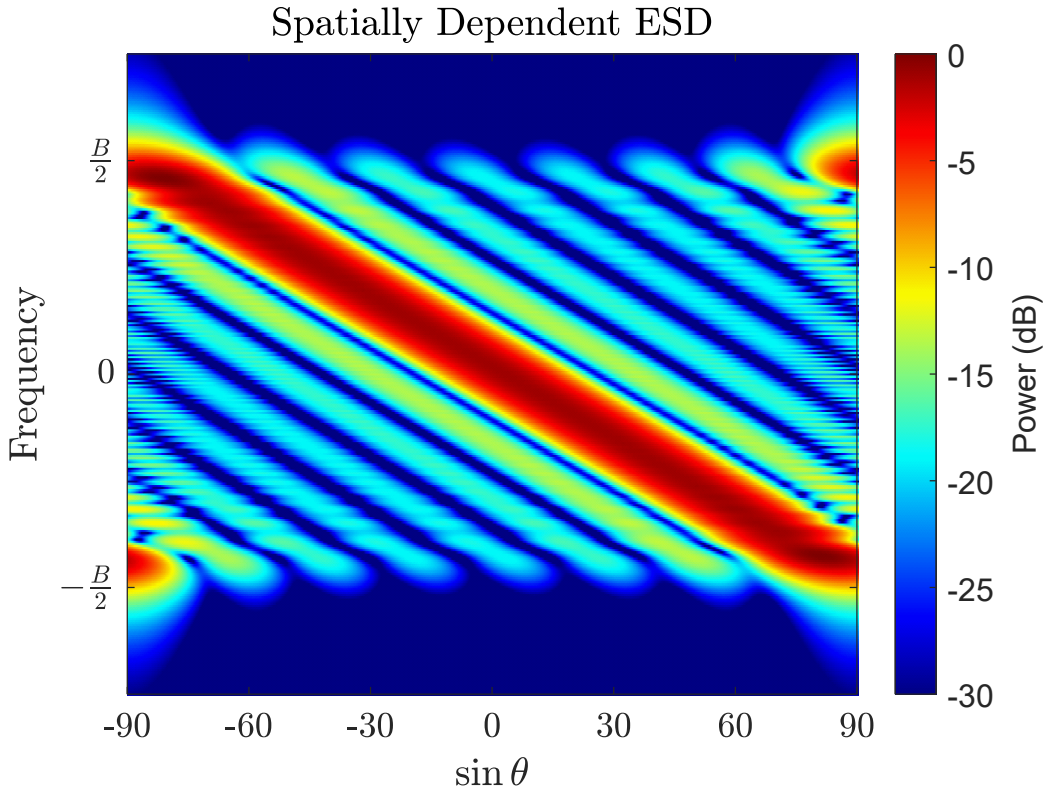

Figure 2.3: Energy Spectral Density for the LFMCW-FDA emission, $\phi_o = -\pi$, $\Delta F = 1/T$, $M = 8$

Looking at Figure 2.3, it is important to note that the bandwidth transmitted in any given spatial direction is reduced, which can be clearly observed by taking a spatial cut, at any angle, across frequency.

Due to the sweeping nature across space for either time or frequency, the term sweep will from here on refer to either, and likewise the term Sweep Repetition Frequency (SRF) will be used to describe the rate of sweeping in either dimension:

$$SRF = \Delta F = \frac{1}{T} \tag{2.8}$$

2.3 LFMCW-FDA Emission For Search Radar

As previously discussed, a primary objective for a search radar is the illumination of a large spatial extent. As seen in the previous section, the FDA structure inherently accomplishes this objective,

without the need for phase shifters or mechanical steering. With this in mind, the LFMCW-FDA presents an attractive emission structure for use in a search context. While not the primary focus of this work, the potential of the LFMCW-FDA emission structure used for search and track is briefly explored here, and could easily be a primary candidate for future application focused work.

Traditionally, search radars accomplish the illumination objective by employing a scanning pattern, determined by dividing the extent of spatial coverage into sections using the beamwidth of the transmit antenna. The beam is focused at a particular spatial angle for a period of time sufficient to estimate scattering parameters. The beam is then focused to the next spatial angle and the process repeats. In this sequential manner, the entire spatial extent is covered.

2.3.1 Revisit Rate

The rate at which scattering parameters are updated for a particular range, angle and Doppler bin is referred to here as the revisit rate. Two approaches to the choice of this rate are under consideration, sourced from [12].

The Track-while-Search (TWS) approach maintains a constant revisit rate for all spatial angles, and thus does not deviate from the scan pattern employed. The Search-and-Track (SAT) approach allows for the reallocation of radar resources to update the profile of a scatterer at a particular spatial angle based on assessed threat along with other factors. For example, this could take the form of interleaving an extra dwell or two at the last known scatterer spatial location within the scan pattern itself. In this case, the revisit rate for the other spatial angles is reduced, as more time is allocated to the particular spatial angle of interest. The effective ability to search the rest of the spatial extent suffers. At the extreme, scatterer overload could diminish the ability to search the entire volume of space in an adequate and timely manner.

Interestingly, the FDA emission essentially provides the TWS approach inherently, within the fast-time. The FDA emission illuminates the entire spatial extent at the SRF, and so the revisit rate for all spatial angles would be an integer multiple of the sweep rate. The time T_{rev} between measurements would thus be an integer multiple of the single sweep time $1/SRF$:

$$T_{Rev} = N \cdot \frac{1}{SRF} \tag{2.9}$$

Where N is determined by the amount of sweeps necessary to achieve acceptable detection performance.

One can imagine a scenario where the SRF can be changed on the fly, in which case the revisit rate can be altered accordingly. Due to the sweeping structure, scattering from all angles are updated at this increased rate simultaneously. Thus, a FDA emission could potentially accomplish the two goals at once: increase the revisit rate when deemed necessary, while also maintaining the ability to estimate parameters across the entire spatial extent simultaneously, effectively not sacrificing the search for the track. Increasing the SRF comes with a reduction in the unambiguous range from (1.4).

2.3.2 Swept Transmit Power

Due to the sweeping nature of the mainbeam across a fast-time interval T, the amount of RF energy placed on a scatterer at any given spatial angle is reduced relative to an emission which stays focused on a single spatial angle over the same time interval. Thus, it becomes important to know the expected average transmit power in any one spatial direction for the FDA emission. While a detector will not be discussed in this work, suffice it to say that the average power transmitted for a single sweep informs the number of sweeps N required to achieve a desired probability of false alarm for a later detection stage, directly informing achievable revisit rates from (2.9)

The average power transmitted over a single sweep and spatial direction is computed as follows. To reduce terms for compactness, the transmission at boresight ($\theta = 0^\circ$) will be considered. The far-field signal transmitted in the boresight direction is thus (2.2) evaluated for $\theta = 0$:

$$g(t,0) = \frac{1}{M} \sum_{m=0}^{M-1} s(t) e^{j[2\pi \Delta F t + \phi_0]m} \tag{2.10}$$

The average power of a signal transmitted in a particular spatial direction θ_i can be found by:

$$P = \frac{1}{T}\int_0^T |g(t,\theta_i)|^2\,dt \tag{2.11}$$

By plugging (2.10) into (2.11), using $|g(t)|^2 = g(t)\cdot g^*(t)$, and expanding the summation:

$$P_{FDA} = \frac{1}{TM^2}\int_0^T |s(t)|^2[1+e^{j[2\pi\Delta Ft+\phi_0]}+..+e^{j([2\pi\Delta Ft+\phi_0](M-1))}][1+e^{-j[2\pi\Delta Ft+\phi_0]}+..+e^{-j([2\pi\Delta Ft+\phi_0](M-1))}]\,dt$$

This can be rewritten as (see Appendix B):

$$P_{FDA} = \frac{1}{TM^2}\int_0^T |s(t)|^2[M+\sum_{m=2}^{M} 2(m-1)\cos([2\pi\Delta Ft+\phi_0][M-m+1])]\,dt$$

Assuming a constant amplitude of unity for the waveform, $|s(t)|^2 = 1$. Integrating yields:

$$P_{FDA} = \frac{1}{TM^2}[M\cdot T+\sum_{m=2}^{M} 2(m-1)\sin([2\pi\Delta FT+\phi_0][M-m+1])] \tag{2.12}$$

For a given M, the resulting transmitted power is determined by the rate of sweeping ΔF and phase offset ϕ_0. For the LFMCW-FDA emission, $\Delta F = 1/T, \phi_0 = -\pi$. Plugging these values into (2.12), the phase values of the sin() term all become integer multiples of π, which results in the whole summation term equating to zero. Thus,

$$P_{FDA} = \frac{1}{TM^2}[M\cdot T+0] = \frac{1}{M}$$

Interpreting this result, M sweeps (and thus $M\cdot T$ time intervals) will be required to achieve the same amount of average power as the non-sweeping case (energy focused in one spatial direction). Thus the tradeoff for persistent illumination within the fast-time is a reduced average transmitted power in any given spatial direction. Depending on the context and desired performance, the LFMCW-FDA emission could provide a beneficial alternative to traditional search radars. The benefit of this structure lies within the ability to vary the revisit rate for all spatial locations simultaneously, provided the reduced average transmit power on a sweep to sweep basis is acceptable, along with the varying unambiguous range resulting from varying the revisit rate.

Chapter 3

Single Channel Receive Processing

3.1 Receive Signal Model

The receive signal $y(t)$ for a receiver co-located with the transmit antenna can be modeled as a time-delayed, Doppler shifted and complex scaled version of the emission $g(t,\theta)$, where the p^{th} point scatterer is located at a time delay τ_p, spatial angle θ_p, with Doppler frequency f_{D_p} and complex scaling γ_p:

$$y(t) = \sum_{p=0}^{P-1} \gamma_p g(t-\tau_p, \theta_p) e^{j2\pi f_{D_p} t} \tag{3.1}$$

To simplify, consider a single sweep ($N = 1$) for the case of a single, non-moving point-scatterer ($P = 1, f_{D_o} = 0$). This simplifies 3.1 to

$$y(t) = \gamma_o g(t-\tau_o, \theta_o) \tag{3.2}$$

3.2 Correlation with Unshifted LFM

The receive signal $y(t)$ is correlated with an **unshifted** LFM chirp $s(t)$, where the correlation response $\hat{x}(\tau)$ can be expressed as:

$$\hat{x}(\tau) = \frac{1}{T} \int_{-\infty}^{\infty} s^*(t-\tau) y(t) dt \tag{3.3}$$

Plugging in the expressions (2.2) and (3.2) and rearranging:

$$\hat{x}(\tau) = \gamma_o \sum_{m=0}^{M-1} e^{-j\pi m} e^{j\pi \sin(\theta_o) m} \frac{1}{T} \int_{-\infty}^{\infty} s^*(t-\tau) s(t-\tau_o) e^{j2\pi m(t-\tau_o)/T} dt$$

As shown in Appendix A, the correlation response can likewise be expressed as a summation of slices of the LFM-ambiguity function, evaluated across delay at particular frequency offsets:

$$\hat{x}(\tau) = \gamma_o \sum_{m=0}^{M-1} A(\tau - \tau_o, \frac{m}{T}) e^{-jm\pi} e^{\pi \sin(\theta_o) m} \tag{3.4}$$

Where the ambiguity function is defined as

$$A(\tau, f_d) = \frac{1}{T} \int_0^T s^*(t-\tau) s(t) e^{j2\pi f_d t} dt$$

The expression of (3.4) can be simplified further, by noting that the delay-Doppler ridge of the LFM's ambiguity function can be approximated as delayed copies of the LFM autocorrelation $A(\tau, 0)$, along with additional phase rotation terms (see Appendix A for more on the added phase rotation):

$$A(\tau, \frac{m}{T}) \approx A\left(\tau + \frac{m}{B}, 0\right) e^{-j\pi \frac{m^2}{BT}} e^{j\pi m} \tag{3.5}$$

Plugging (3.5) into (3.4), the correlation response can now be approximated as:

$$\hat{x}(\tau) \approx \gamma_o \sum_{m=0}^{M-1} A\left(\tau - \tau_o + \frac{m}{B}, 0\right) e^{-j\pi \frac{m^2}{BT}} e^{\pi \sin(\theta_o) m} \tag{3.6}$$

Due to the particular frequency offset spacing $\Delta F = 1/T$, the correlation peak of one waveform is separated in delay a distance of $\pm 1/B$ from the adjacent peaks, and thus is in a null of all the other responses, allowing the ability to separate each individual waveform. This structure is also known as a virtual array, as all the reflected transmit waveforms are present and separable. The orthogonality of the individual waveforms can be seen in the correlation response of Figure 3.1. Analytically, evaluating (3.6) for $\tau = \tau_o - \frac{k}{B}$, the expression turns into:

$$\hat{x}(\tau_o - \frac{k}{B}) \approx \gamma_o \sum_{m=0}^{M-1} A\left(\frac{m-k}{B}, 0\right) e^{-j\pi \frac{m^2}{BT}} e^{\pi \sin(\theta_o) m} \tag{3.7}$$

For $k \neq m$, the term $A(\frac{m-k}{B}, 0) \approx 0$, so all summation terms other than the $m = k$ term are effectively zero. For the normalized ambiguity function, $A(0,0) = 1$. With this, the expression can be rewritten:

$$\hat{x}(\tau_o - \frac{k}{B}) \approx \gamma_o e^{-j\pi \frac{k^2}{BT}} e^{2\pi \frac{F_c}{c} kd \sin(\theta_o)} \tag{3.8}$$

Looking at (3.8), the spatial information from the scatterer at θ_o imparted to the k^{th} waveform is present, along with the appropriate scaling γ_o and an additional undesired phase rotation term, denoted as the "video phase", which will be explored momentarily.

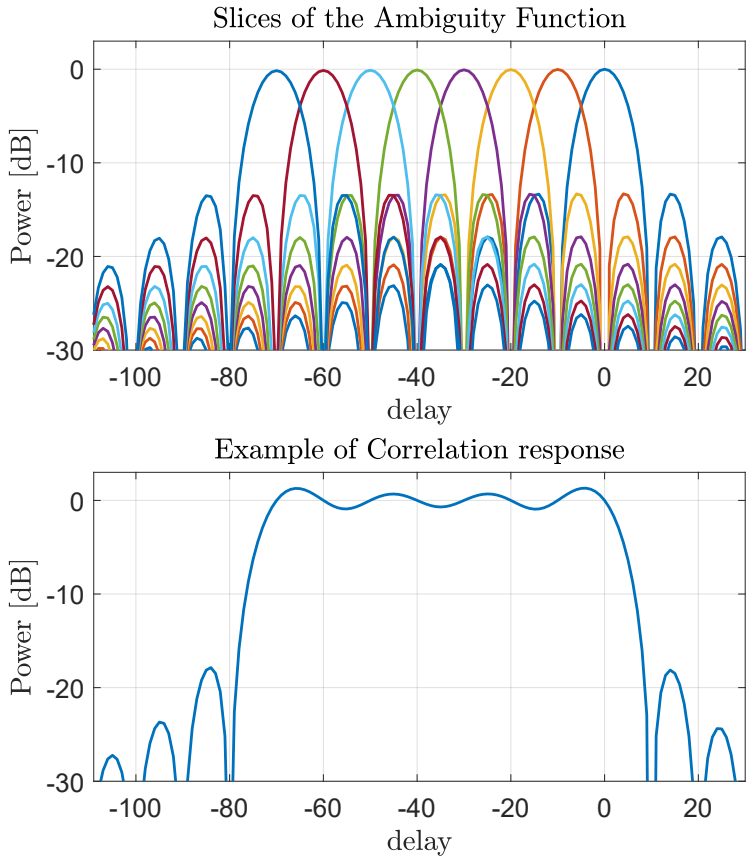

Figure 3.1: Ambiguity function slices (top) and example correlation response (bottom), with over-sampling factor for display purposes

3.2.1 Formation of the Virtual Array in Delay

Figure 3.1 visually shows the expected structure of the virtual array in delay, **for the particular emission structure where an up-chirp and positive ΔF's are transmitted, and the unshifted LFM is used as the correlation filter**. Depending on the combination of up/down-chirp and $\pm\Delta F$, the virtual array could form on a different side of the zero delay point, and/or have the ordering of the peaks change.

For the fixed element indexing of $[0 : M-1]$, where $M = 8$, the possible combinations of $\pm\Delta F$ and up/down-chirps are shown below, with the corresponding virtual array formed after correlating with the unshifted LFM or $m = 0$ waveform.

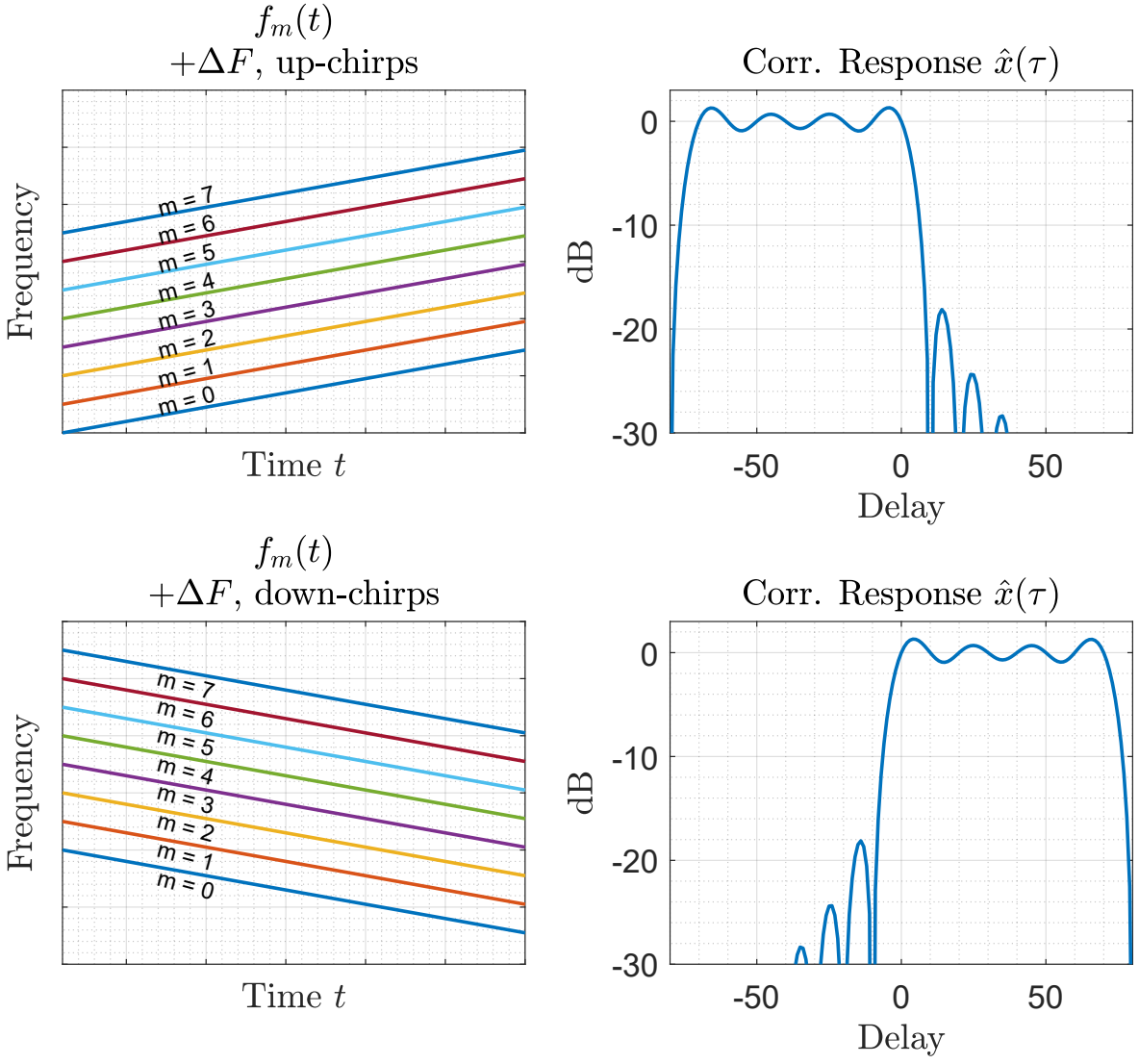

Figure 3.2: Differing combinations of positive ΔF with up/down chirps, and the resulting virtual array structure. $f_m(t)$ is the instantaneous frequency function for the m^{th} transmit waveform

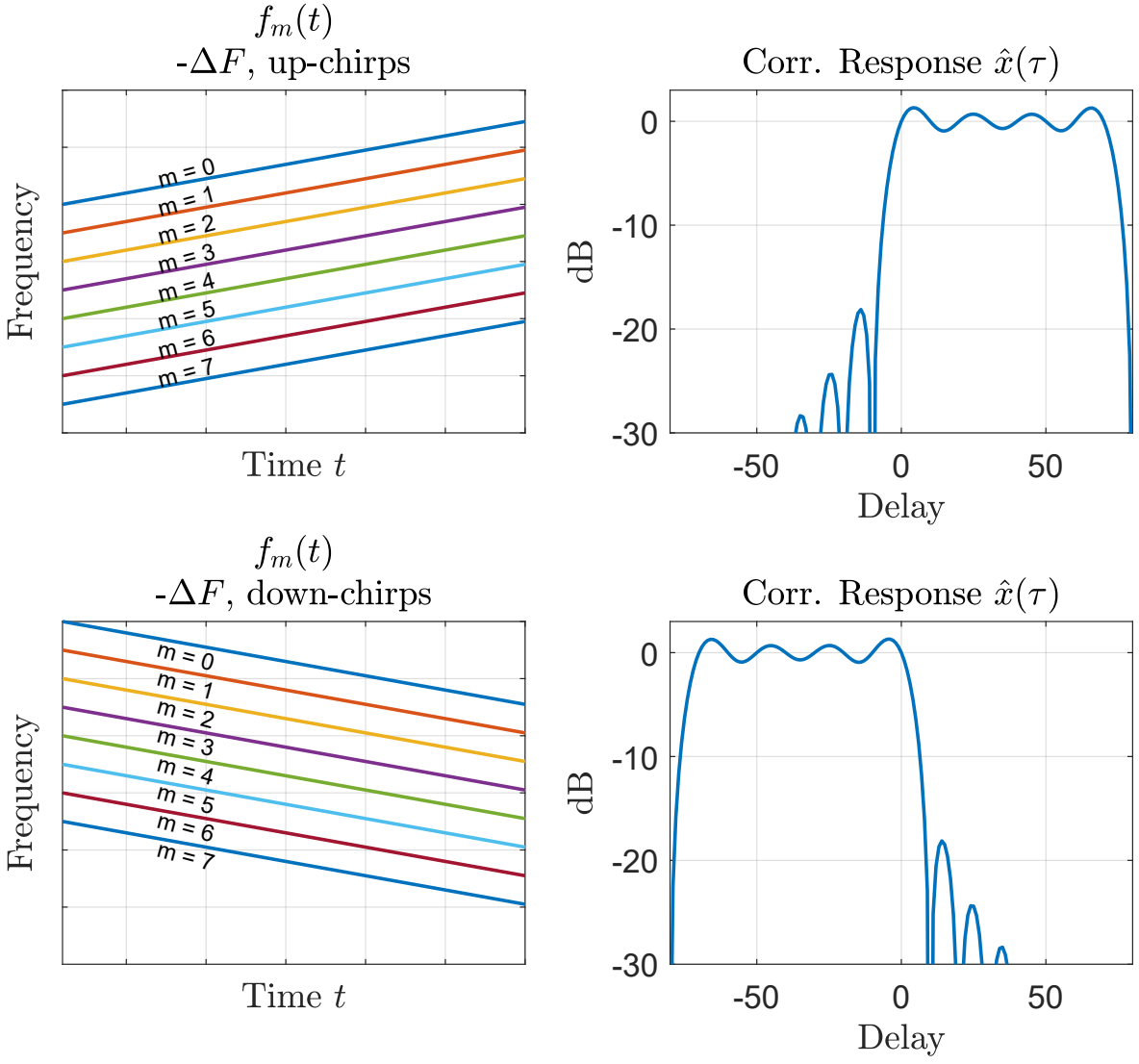

Figure 3.3: Differing combinations of negative ΔF with up/down chirps, and the resulting virtual array structure. $f_m(t)$ is the instantaneous frequency function for the m^{th} transmit waveform

3.2.2 Video Phase

As equation 3.8 shows, the k^{th} peak has the k^{th} element-wise phase rotation associated with a scatterer at θ_o. However, alongside this term is an additional phase rotation, which is dependent on BT and k. This term will be referred to as the video-phase term, named such with reference to a similar term resulting from stretch processing [13].

The impact of the video phase term on the estimate of θ_o is shown below in Figure 3.4.

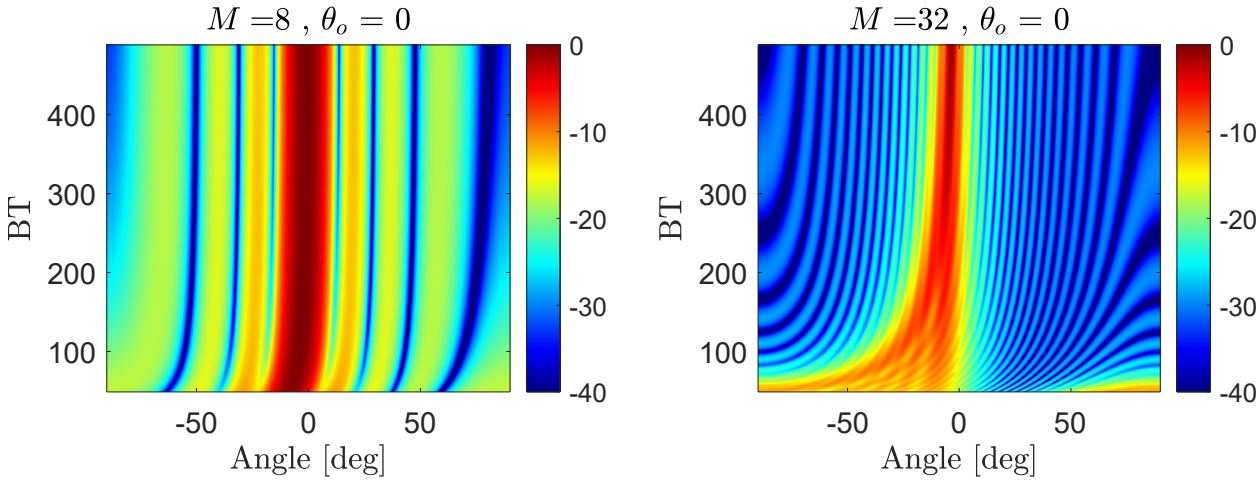

Figure 3.4: Beamforming of the video phase term, for differing M

By beamforming just this video phase term, an expected error can be seen from this response, visually shown in the Figure 3.4. Note that for increasing BT, the expected video phase error is reduced (for a constant M).

Because of the known structure of this video phase term, we can easily correct for it once the correlation processing and virtual channel shaping has occurred, by simply applying the conjugate phase term to the corresponding virtual channel:

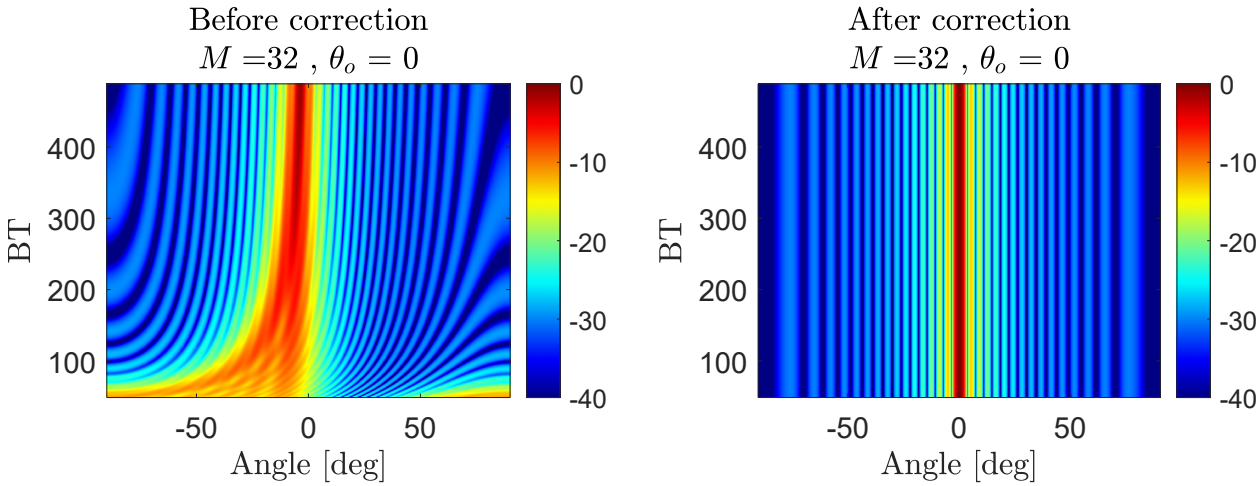

Figure 3.5: Beamforming responses, before and after correcting the video phase term

3.3 Beamforming Virtual Channels

With the virtual array formed in the correlation response along the delay dimension, the response can be reshaped to form M virtual channels, where the k^{th} channel is formed by delaying the correlation response by $\frac{k}{B}$, aligning each element of the virtual array over the scatterer delay τ_o. These responses can then be beamformed, and the video phase term can be corrected by likewise adding the conjugate of the term, to form the range-angle estimate $\hat{x}(\tau,\theta)$:

$$\hat{x}(\tau,\theta) = \sum_{k=0}^{M-1} \hat{x}(\tau - \frac{k}{B}) e^{j\pi \frac{k^2}{BT}} e^{j\pi \sin(\theta) k} \tag{3.9}$$

The expected delay-angle response for a scatterer at $\theta_o = 0^\circ$ can be seen in Figure 3.6:

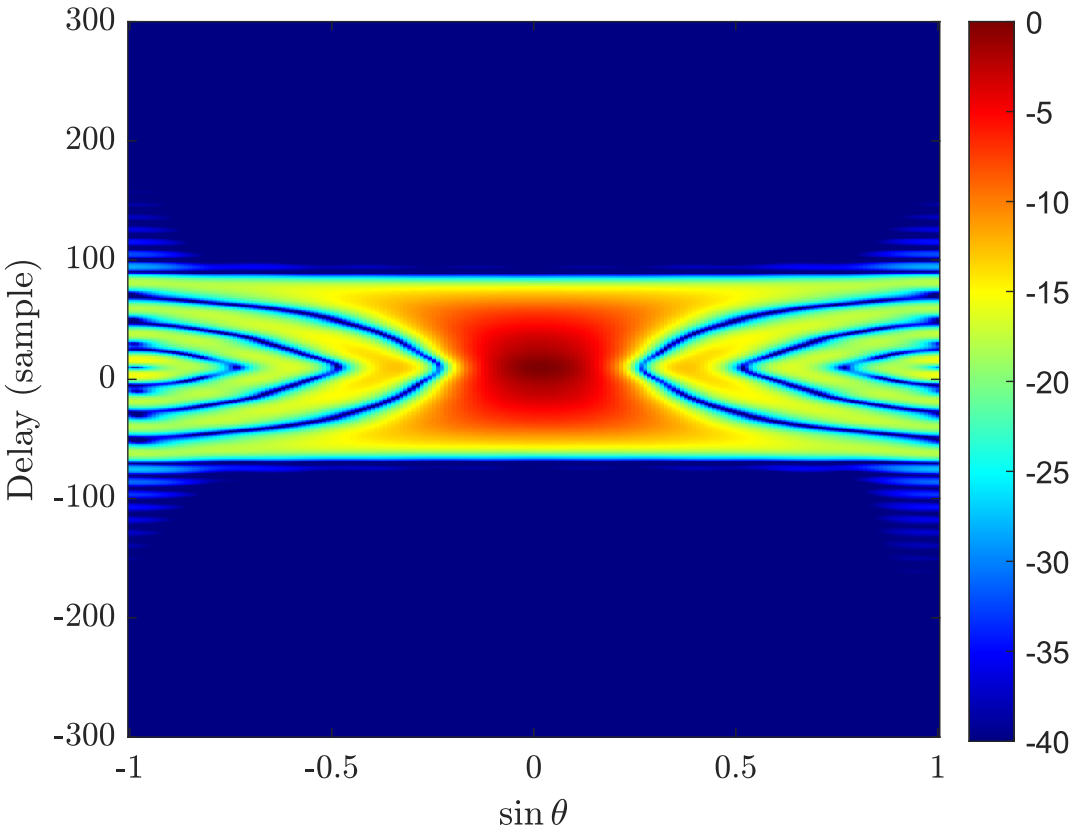

Figure 3.6: LFMCW-FDA MISO Ambiguity Function

Taking a cut across the spatial dimension for zero delay, the expected spatial resolution can be

visualized:

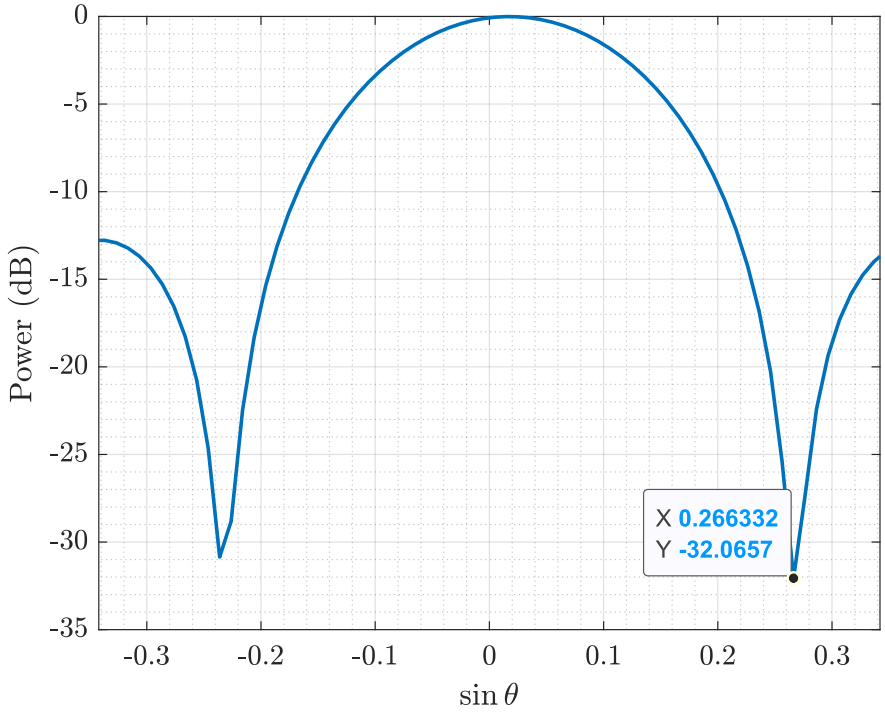

Figure 3.7: LFMCW-FDA MISO Spatial Resolution

From Figure 3.7, the peak to null beamwidth is about 0.266 in $\sin\theta$ space. Calculating the expected spatial resolution for a ULA of $M = 8$ elements spaced $d = \frac{\lambda_c}{2}$, using (1.10)

$$\Delta\theta \approx \frac{2}{7} = 0.2857 \text{ rad} \tag{3.10}$$

Converting this to degrees and then $\sin\theta$, $\Delta\sin\theta = 0.2818$. As the expression of (1.10) is an approximation, this result shows that the beamwidth of the transmit antenna composed of $M = 8$ elements is effectively retained by the MISO LFMCW-FDA system.

Up to this point, continuous time models have been used to explicitly show the intricacies of the math involved. In a real system, the continuous signal $y(t)$ is sampled to form a vector $\mathbf{y}[n]$ at sampling rate $f_s = B$. While this looks like critical sampling, recall from Figure 2.3 that in any given spatial direction the transmitted bandwidth is reduced by a factor of M.

The data vector $\mathbf{y}[n]$ is correlated with the unshifted waveform to form the correlation response $\hat{\mathbf{x}}[l]$, shown in Figure 3.8.

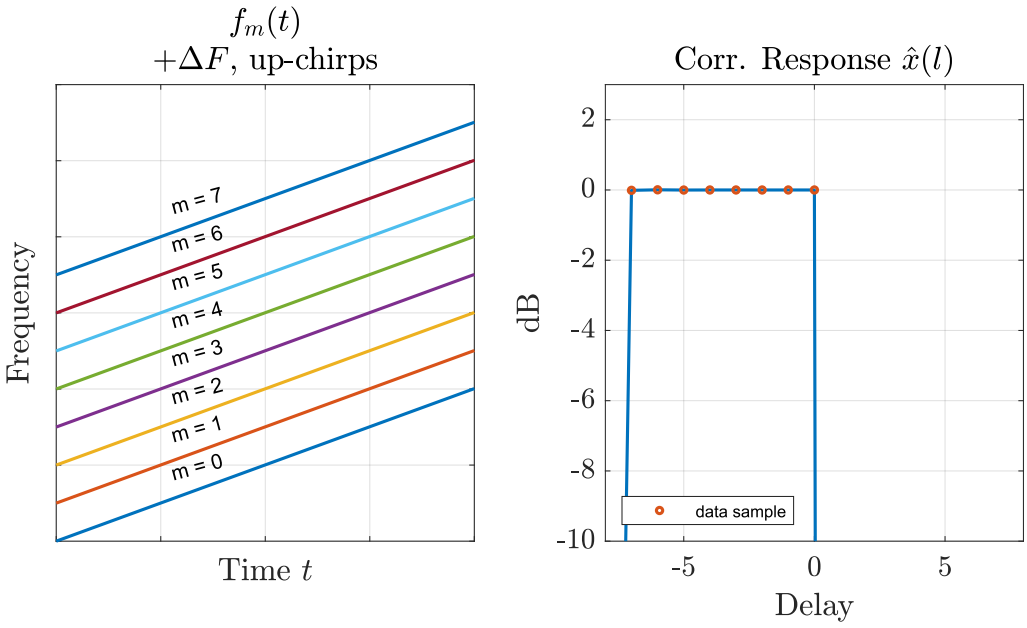

Figure 3.8: Instantaneous frequency function chosen for the MISO LFMCW-FDA system (left) and resulting virtual array structure (right), critically sampled

The sampled correlation response results in the peaks for each waveform response being separated by a single sample. The k^{th} virtual channel is thus formed by circ-shifting $\hat{\mathbf{x}}[l]$ by k samples.

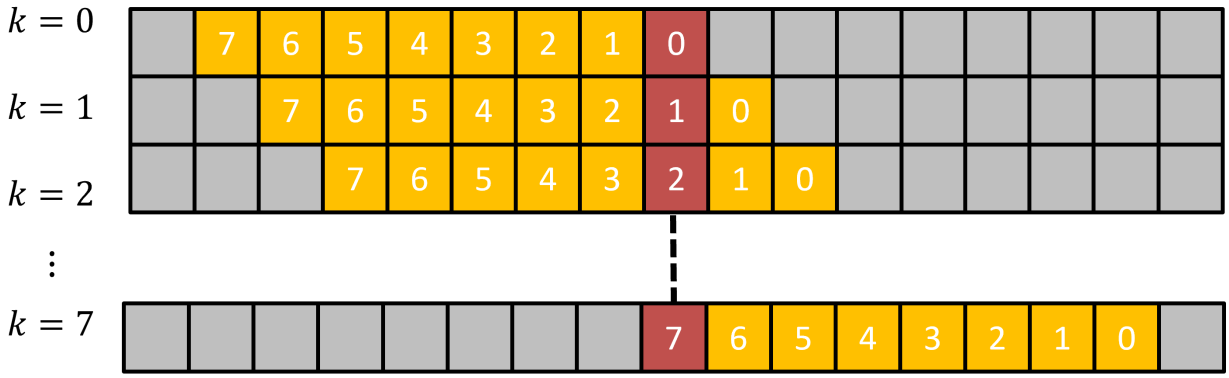

Figure 3.9: Formation of k virtual channels

The delay-compressed receive data for a single sweep is now in the form of an MxN data

matrix.

3.3.1 Range and Doppler Performance

A full CPI's worth of data is chopped up into individual sweeps, and the process of reshaping is performed to achieve a data cube. From here, Doppler processing can be performed.

The unambiguous range R_{ua} for LFMCW-FDA depends on the sweep time T, which also means it can be related to the SRF from (2.8) as

$$R_{ua} = \frac{cT}{2} = \frac{c}{2SRF} \tag{3.11}$$

The range resolution ΔR for this emission is degraded due to the decreased bandwidth in any one spatial direction, as seen in Figure 2.3. Further, the correlation responses for a single point scatterer show clearly the extended response is a function of M waveforms, and so are factored in as

$$\Delta R = M \cdot \frac{c}{2B} \tag{3.12}$$

As mentioned in the first section, the FDA and DDMA emissions are similar, differing only by ΔF. Critically, in the LFMCW-FDA case the Doppler responses from each waveform wrap back onto the Doppler response of the unshifted $(m = 0)$ waveform, retaining the full unambiguous Doppler space. Thus, $f_{d_{ua}}$ is simply tied to the SRF

$$f_{d_{ua}} = SRF = \frac{1}{T} \tag{3.13}$$

Finally, the Doppler resolution Δf_d is dictated by the integration time T_{CPI} as

$$\Delta f_d = \frac{1}{T_{CPI}} \tag{3.14}$$

Even though the transmit system is CW, a process similar to PRF staggering in pulsed systems

can be implemented on this received data to increase the unambiguous range and Doppler spaces. It has been shown in work using the same MISO LFMCW-FDA system that by altering the sweep repetition frequency (SRF) on a CPI-to-CPI basis, ambiguous returns in range and Doppler can be resolved. This work is not discussed here.

3.4 Simulation Results

To demonstrate the capabilities and limitations of the MISO LFMCW-FDA system, simulations involving point scatterers at various range, Doppler and spatial angles were generated, and the resulting receive processed parameter estimates are presented. Table 3.1 shows the operating parameters used for this simulation. These parameters mirror those used in the open-air data collected and processed, with those results presented in the following section. DDMA and TDMA emissions for the same scene and operating parameters are also shown, to demonstrate the advantages that the MISO LFMCW-FDA system provides in comparison.

Note that the ADC rate here was based on the experimental system transceiver ADC. LFM bandwidth B was chosen relative to this ADC rate, as ADC rate $= 3B$.

The expected range and Doppler performance metrics are summarized in Table 3.2, and can be found easily by plugging the appropriate values from Table 3.1 into the appropriate metrics equations of (3.11),(3.12),(3.13), and (3.14), from section 2 (see Appendix C for worked through calculations). Frequency offset ΔF was chosen to purposely induce ambiguous returns in range, and this is why the unambiguous velocity is comically large.

Metrics Summary		
Metric	Symbol	Value
Range Resolution	ΔR	14.65 m
Unambiguous Range	R_{ua}	732 m
Velocity Resolution	Δv_d	4.55 m/s
Unambiguous Velocity	$v_{r_{ua}}$	9,309.1 m/s

Table 3.2: Summary of MISO LFMCW-FDA Metrics

Table 3.1: Summary of Operating Parameters

Description	Value
Center Frequency F_c	3.3 GHz
LFM Bandwidth B	81.92 MHz
Sweep time T	4.8828 μs
Frequency offset ΔF	204.8 kHz
CPI Duration T_{CPI}	10 ms
Number of Sweeps	2048
ADC rate	245.76 MHz
DSP sampling rate F_s	81.92 MHz
Transmit Channels M	8
Receive Channels	1

For the simulation, constant velocity point scatterer models were used. Scattering RCS for all scatterers were set equal and arbitrarily, with R^4 losses included. White Gaussian noise was added to the receive data, and a receive clutter notch was included in the Doppler processing to simulate typical procedure. An oversampling factor on receive was used as well purely to make the resulting figures more visually appealing to the reader. Doppler was converted to velocity in meters/second to make the results more physically meaningful.

The simulation scene showing the true range, velocity and spatial angle of the 4 scatterers placed in the scene are shown in Figure 3.10. Note that the two scatterers placed at 275 m and 300 m represent two typical scattering responses well within the unambiguous range of the radar. The scatterer at 710 m was placed as such to show the full use of the unambiguous range space. The scatterer at 850 m is placed outside of the unambiguous range and thus is expected to alias back into the range-velocity map around 850 m - R_{ua} = 118 m

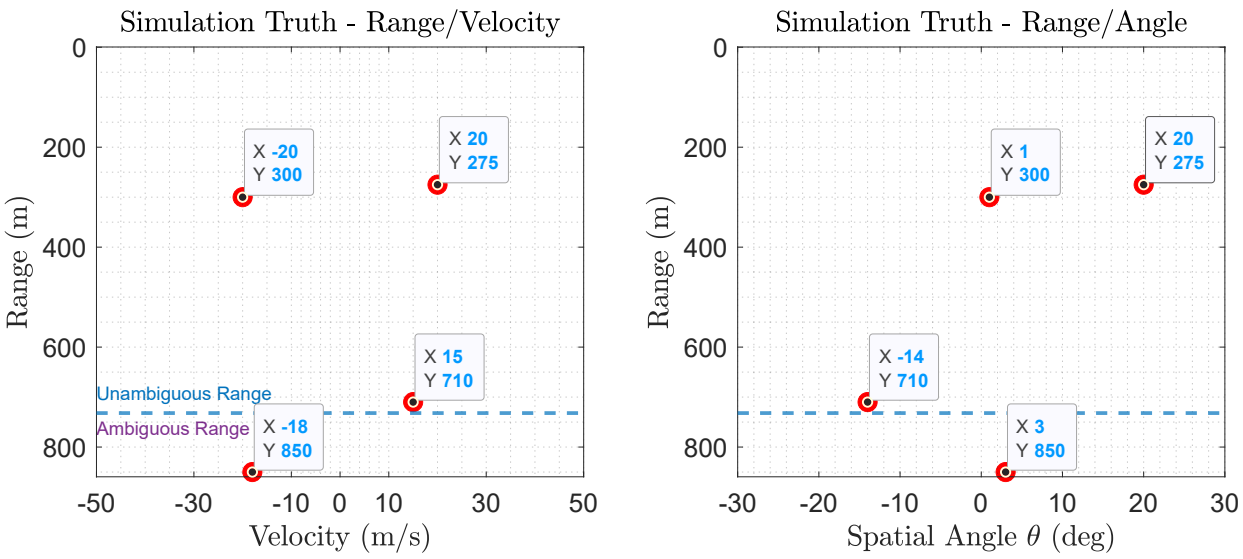

Figure 3.10: Simulation Ground Truth

3.4.1 Range & Doppler Processing

As described in the previous subsections, a full CPI's worth of data is collected with the single receive antenna. This data is correlated with an unshifted LFM, and the responses are chopped up into individual sweeps to form a fast-time x slow-time data matrix. Taking the FFT across slow-time results in a range-Doppler profile. Doppler is then converted to radial velocity via (1.5), and the resulting response is shown in Figure 3.11.

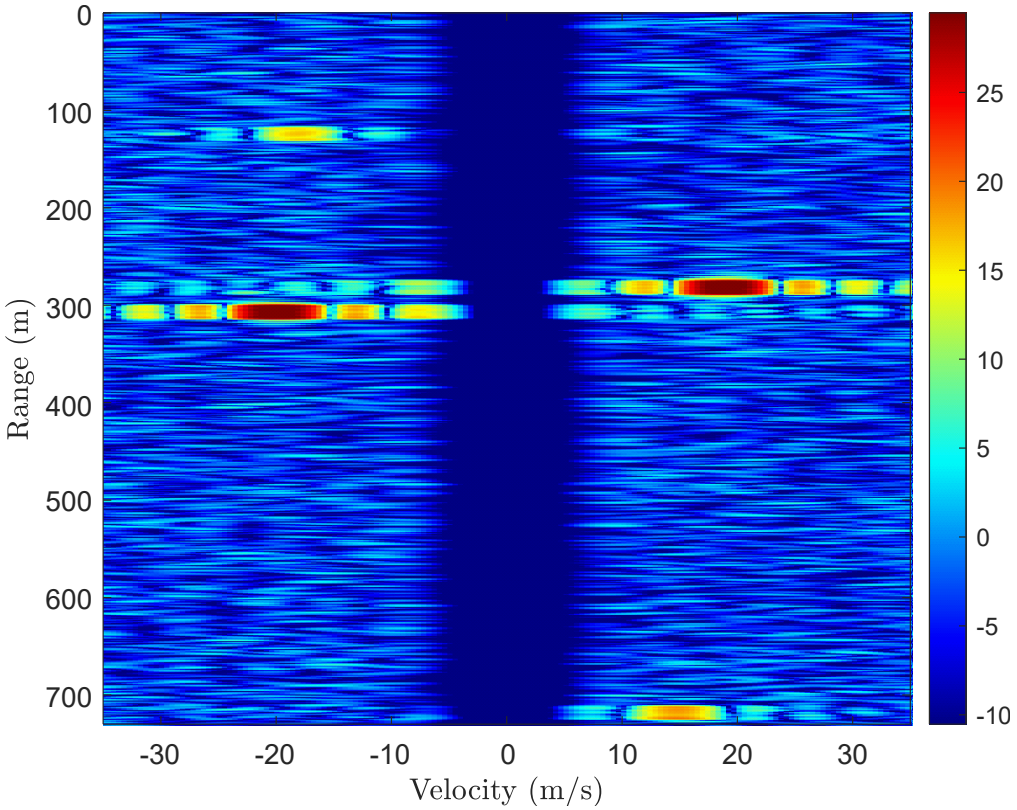

Figure 3.11: Range-velocity map from simulated data (pre-spatial processing)

Looking at Figure 3.11 and comparing with that of the simulation truth of Figure 3.10, scattering locations in range and velocity appear where expected. The scatterer at 850 m indeed aliases back into the expected range area, and the scatterer at 710 m is not aliased, confirming the retention of the unambiguous range for the MISO LFMCW-FDA system.

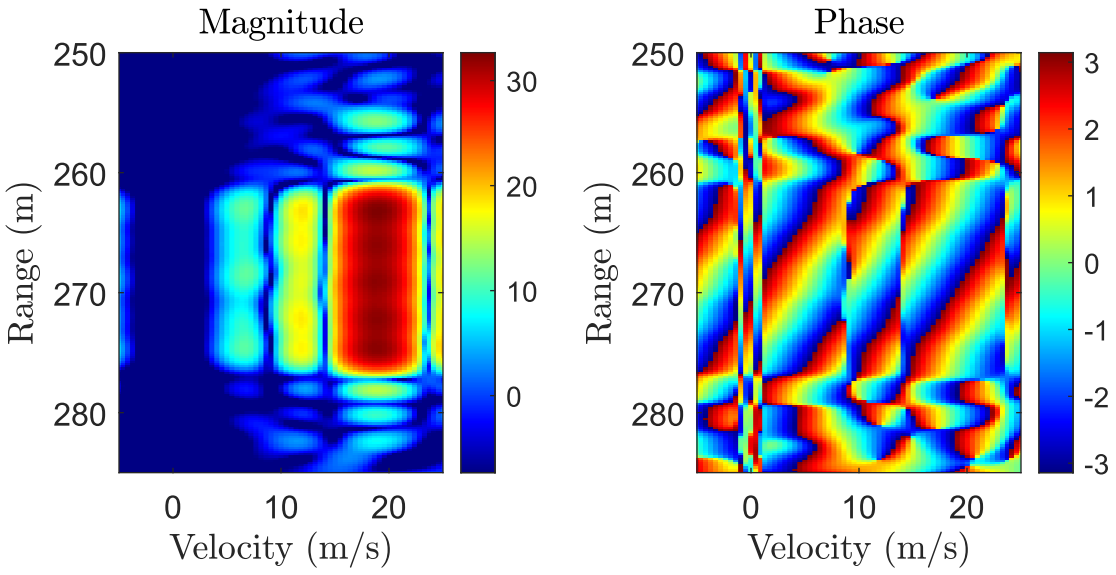

Figure 3.12: Range-velocity maps. pre-spatial processing, in magnitude (left) and phase (right)

Focusing in on the scattering response at 275 m, the left subplot in Figure 3.12 shows the extended range response in magnitude. The last peak response appears at 275 m, and this is consistent with the expected structure of the correlation response for the particular operating parameters of up-chirp with $+\Delta F$ from Figure 3.8 in the previous subsection. The subplot to the right shows the calculated phase angle for the scattering response. The important takeaway from this subplot is the near linear phase progression across the range response of the scatterer. This visually shows the virtual array formed for the scattering after correlation. Zooming into the other scatterers is not necessary as similar responses are seen clearly from Figure 3.11.

3.4.2 Spatial Estimation

After range-Doppler processing, virtual element channels are formed by shifting the correlation responses in delay as previously explained. After forming the virtual channels, beamforming and video phase correction is applied across the virtual channels. The resulting beamformed responses shown are the responses evaluated at the range and velocity locations where the maximum magnitude values occur for each scatterer.

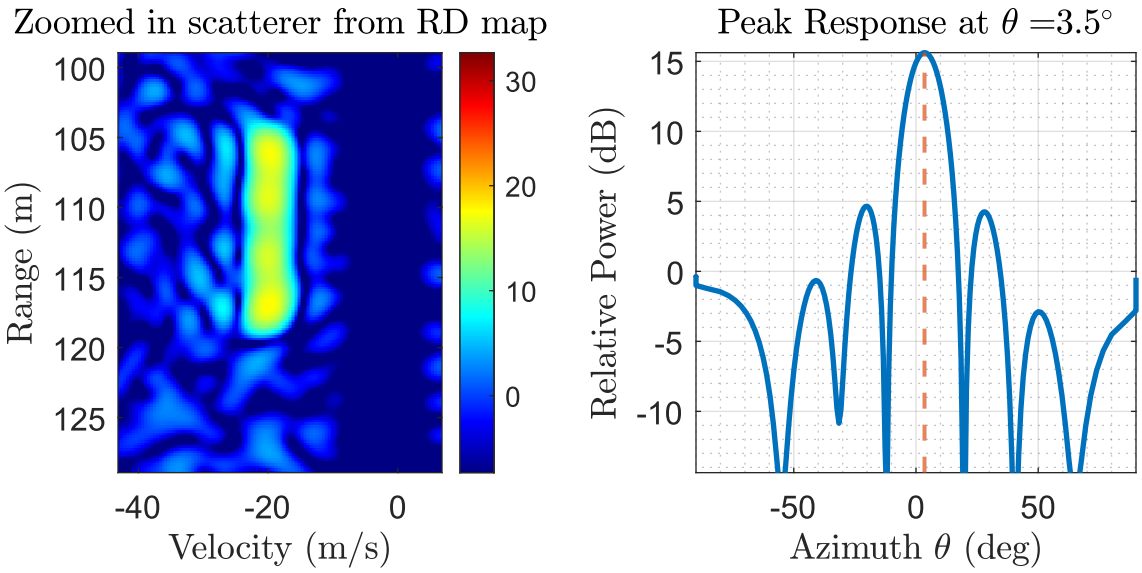

Figure 3.13: Spatially processed response, scatterer aliased from 850 m and -18 m/s

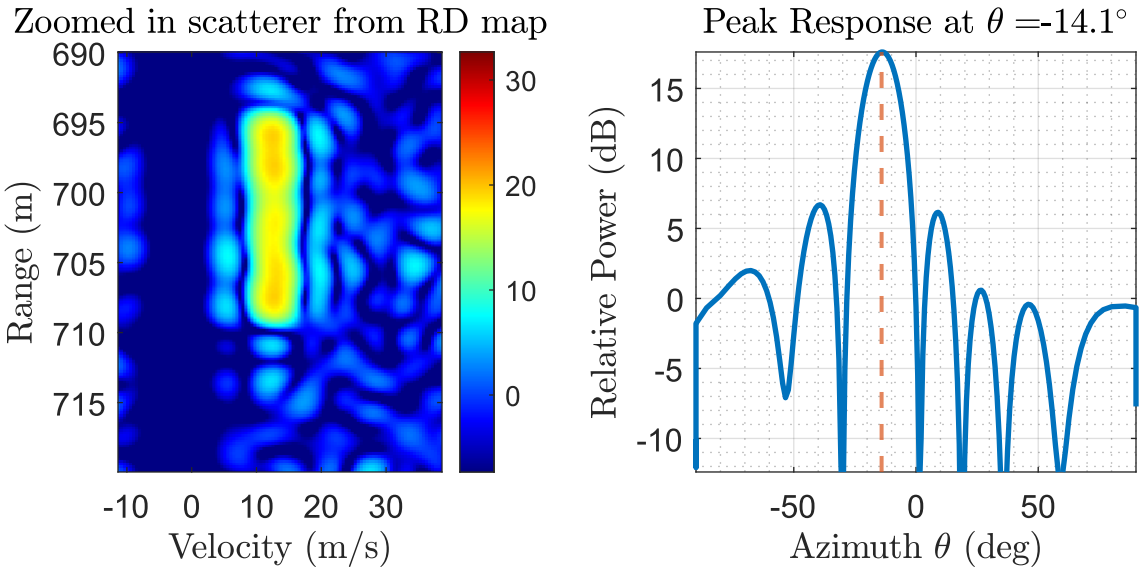

Figure 3.14: Spatially processed response, scatterer at 710 m and 15 m/s

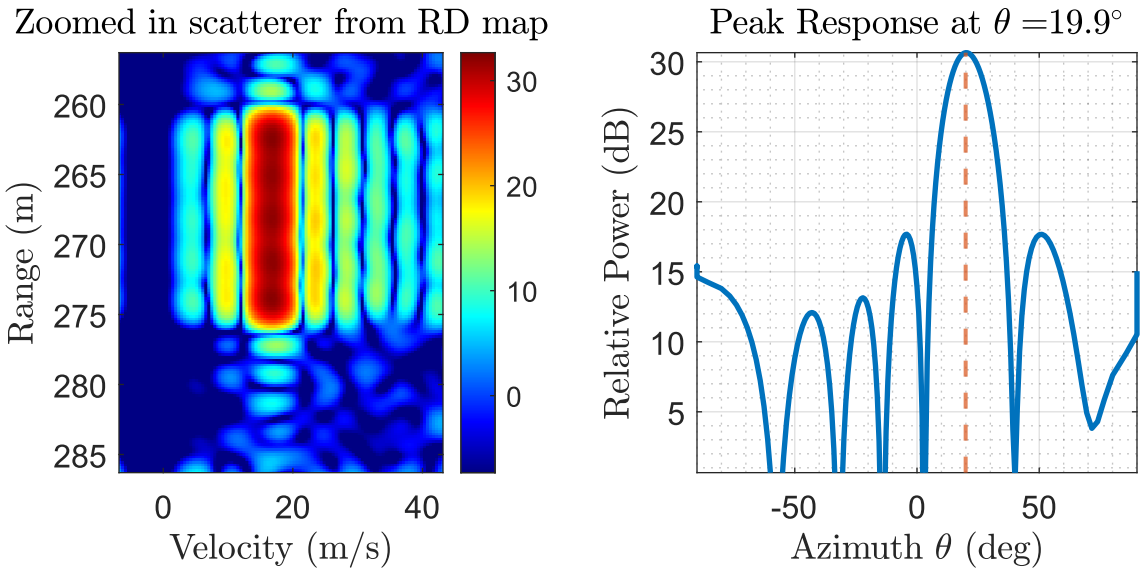

Figure 3.15: Spatially processed response, scatterer at 275 m and 20 m/s

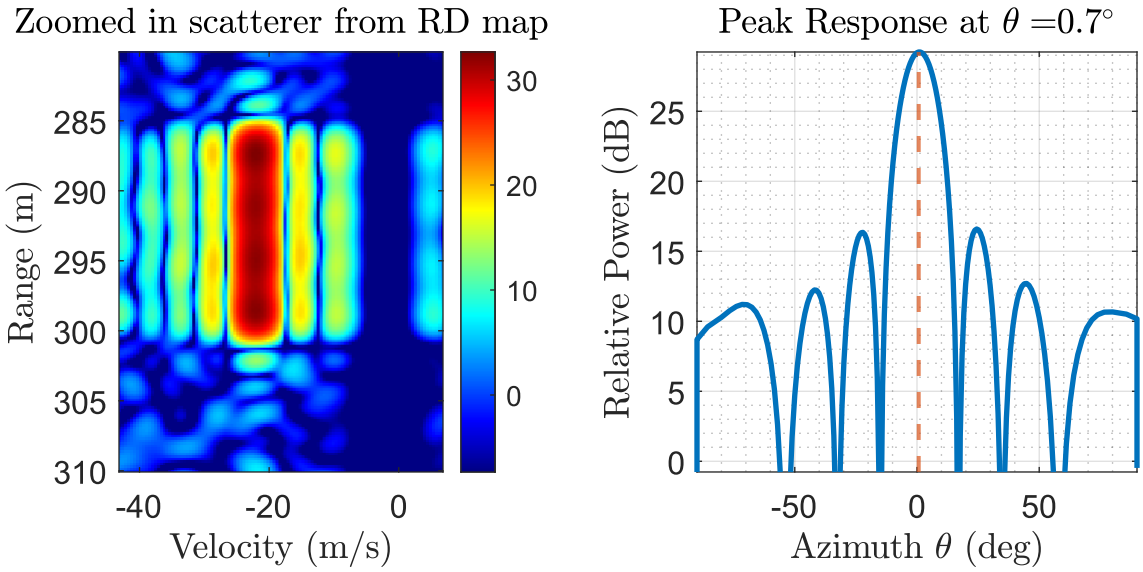

Figure 3.16: Spatially processed response, scatterer at 300 m and -20 m/s

Comparing these Figures to that of the true spatial locations in Figure 3.10, the largest estimate deviation is from the aliased scatterer, with a deviation of 0.5° off of the true spatial location. While not perfect, this performance could still be acceptable for a wide variety of contexts where precise spatial estimation is not critical. Ultimately these results confirm the ability to perform

spatial estimation for the MISO LFMCW-FDA system.

3.5 Comparison to DDMA

To compare the previous range, Doppler, and spatial performance to similar spatially diverse emission structures, both TDMA and DDMA emission structures were transmitted and receive processed in simulation, using the same scene as in Figure 3.10. The main motivation behind this comparison is to demonstrate the lack of versatility in these two emissions when it comes to the unambiguous range and Doppler spaces.

Using the defined emission structure for DDMA from (1.12) and (1.13), the same LFMCW waveform and operating parameters were used from Table 3.1 except that the T_{CPI} was reduced to 1 ms, for visualization purposes, as the responses across the entire Doppler space become difficult to see with that fine of a resolution. The degraded Doppler resolution is still sufficient to see the main comparison point, which is the extended virtual array across the entire Doppler domain, and contributing to the loss in unambiguous Doppler space.

The received data was correlated with the unshifted LFM and reshaped into fast-time x slow-time data matrix, mirroring the correlation procedure previously outlined. The resulting range-velocity map is shown in Figure 3.17.

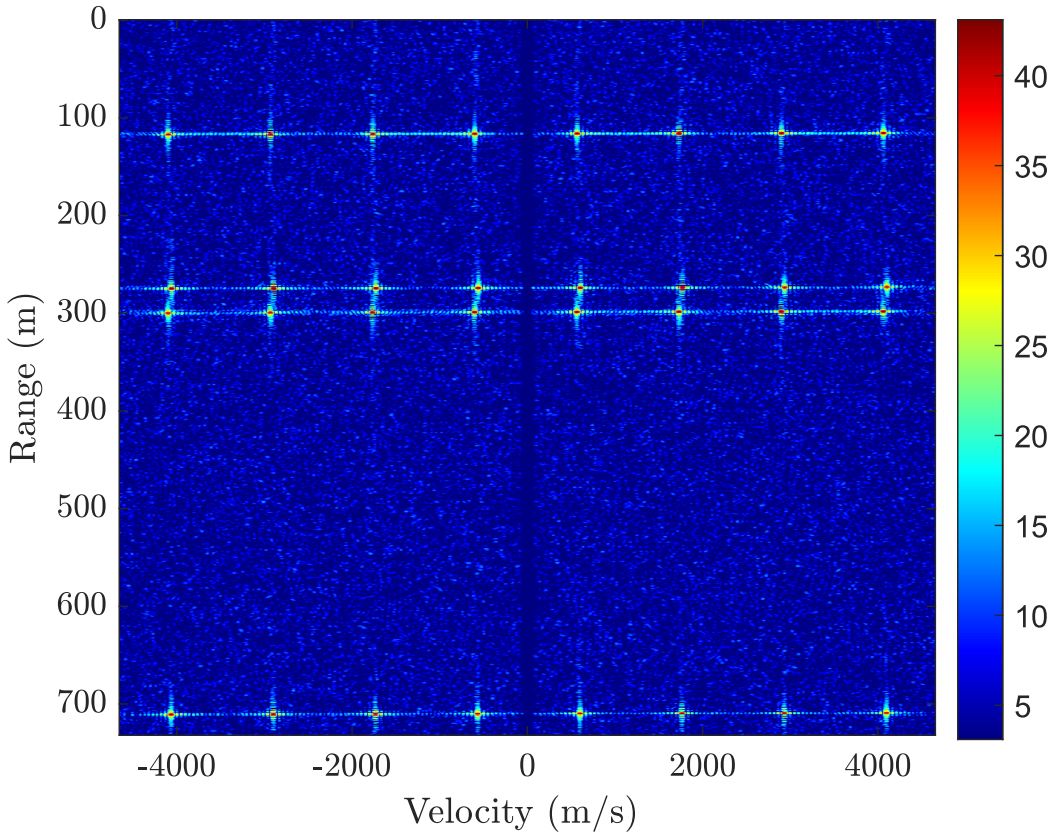

Figure 3.17: DDMA Range-Doppler plot, same scene as for the LFMCW-FDA simulation

As it can be seen from Figure 3.17, the expected virtual array for the DDMA response appears for each scatterer at ranges which appear to agree with the ground truth. Estimating the velocities by observation is less obvious.

Focusing in on the scatterer at 275 m, the Doppler/velocity response at that range bin can be examined:

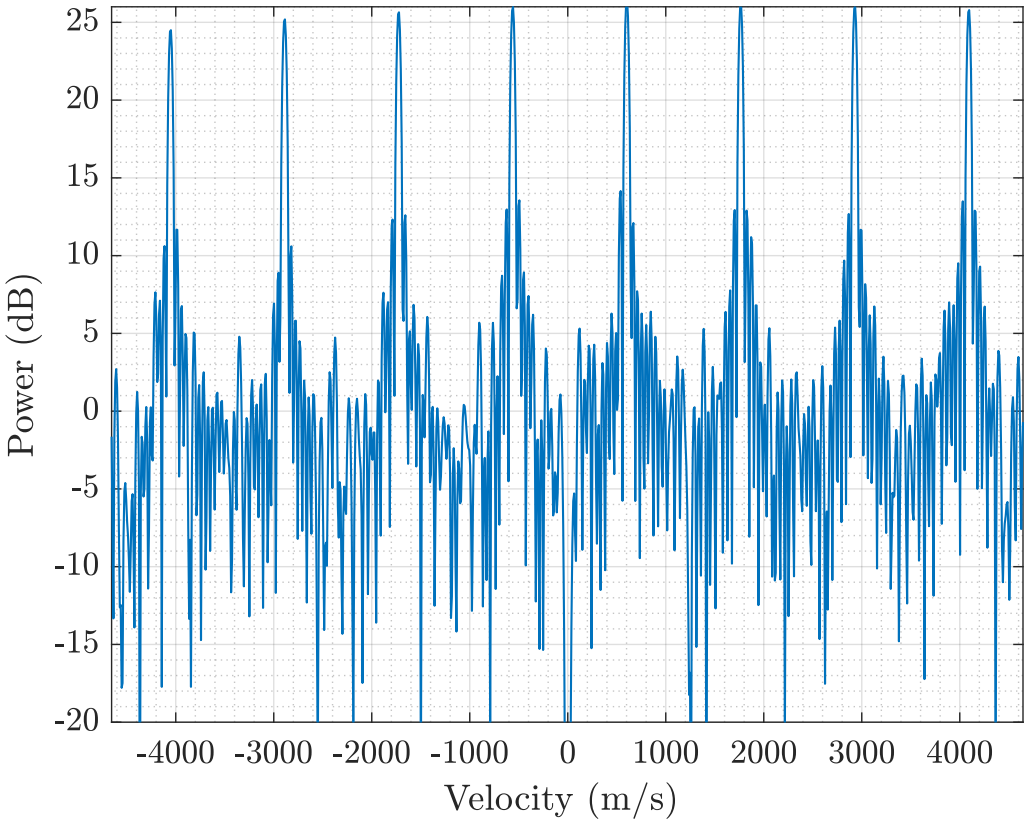

Figure 3.18: DDMA velocity response at range bin of 275 m

The virtual array for the scatterer at 275 m is shown formed along the Doppler/velocity dimension in Figure 3.18. The peaks are separated by the DDMA frequency offset $\Delta F = \frac{1}{MT}$ converted to radial velocity, which is also the unambiguous velocity v_{ua}:

$$v_{ua} = \Delta F \left(\frac{\frac{3x10^8}{3.3x10^9}}{2} \right) = 1,163.6 m/s$$

In order to calculate the Doppler shift/radial velocity for each response, the measured velocity from the m^{th} peak is compared to the m^{th} frequency shift f_m.

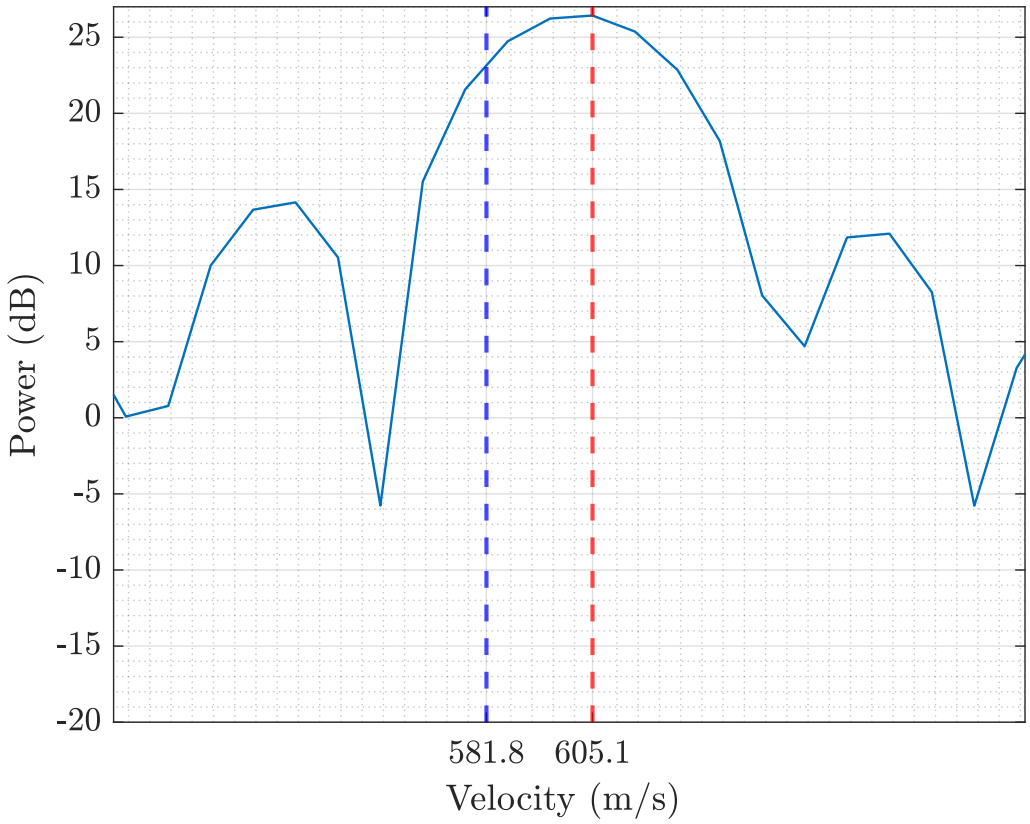

Figure 3.19: Calculating radial velocity of scatterer for DDMA. Blue line indicates the f_4 frequency shift and the red line is the peak of the response

Figure 3.19 shows the velocity response at 275 m zoomed in to the location of the $m = 4$ waveform response. For the m = 4 element, the frequency shift is calculated using (1.13)

$$f_4 = \left(4 - \frac{(8-1)}{2}\right)\left(\frac{1}{(8)(4.8828x10^{-6}}\right) = 12.8 \text{ kHz}$$

Converting this to radial velocity via (1.5)

$$v_4 = f_4\left(\frac{\frac{3x10^8}{3.3x10^9}}{2}\right) = 581.8 \text{ m/s}$$

With the peak response occurring at 605.1 m/s, the estimated velocity would be 605.1 - 581.8 = 23.3 m/s. Due to the order of magnitude difference in integration time between the LFMCW-FDA

results and this result, the lack of Doppler/velocity resolution could easily be deemed as the cause for the 3.3 m/s deviation from the true velocity.

These results show that the DDMA emission with the chosen operating parameters performs sufficiently well for estimating range responses, with the velocity estimating a slightly more involved process. Due to the extreme unambiguous velocity from the high SRF, even when degraded, none of the movers alias. Nonetheless, the unambiguous Doppler space is still clearly reduced, confirming that the LFMCW-FDA emission attains superior Doppler performance with comparison of the unambiguous Doppler/velocity spaces.

3.6 Comparison to TDMA

Using the defined emission structure for TDMA from (1.15), the same LFMCW waveform and operating parameters were used from Table 3.1. The delay offset ΔT was chosen as in [14] as

$$\Delta T = \frac{T}{M} = 0.61035 \ \mu \text{ s} \tag{3.15}$$

After simulating the collection of a full CPI, the same receive processing was performed as for the previous cases. The resulting range-velocity map is shown in Figure 3.20.

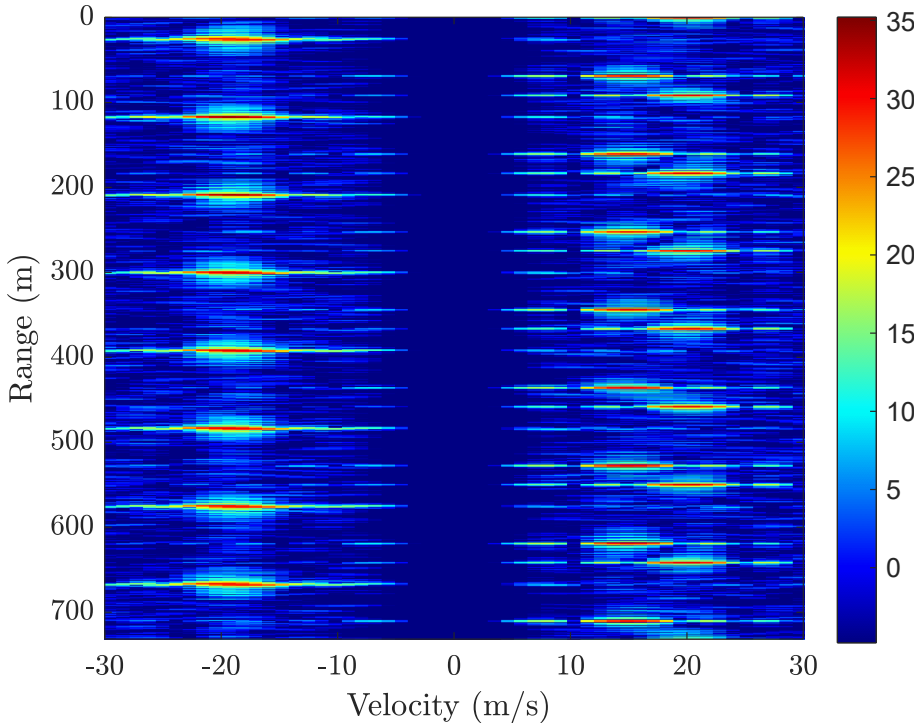

Figure 3.20: TDMA Range-velocity plot, same scene as for the LFMCW-FDA simulation

Observation of Figure 3.20 clearly shows the drawback in using this emission structure for range estimation. Due to the extended virtual array, the unambiguous range R_{ua} is diminished heavily, and is related to ΔT as

$$R_{ua} = \frac{c\Delta T}{2} = 91.55 \text{ m} \tag{3.16}$$

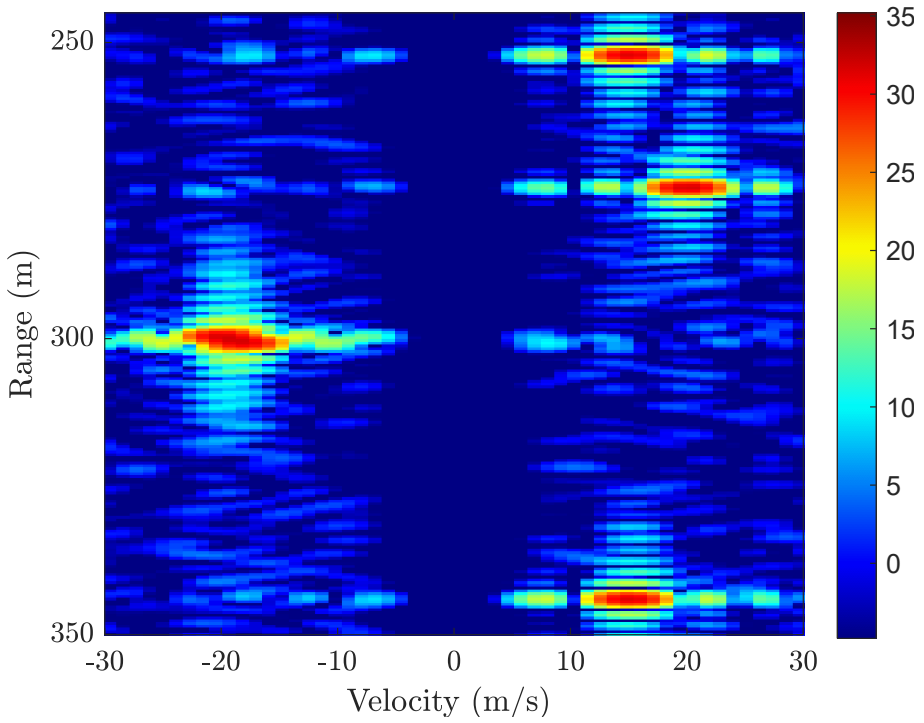

Figure 3.21: TDMA Range-velocity plot, same scene as for the LFMCW-FDA simulation, zoomed in

Figure 3.21 zooms into the response to show what appears to be the scatterers on the negative side of the velocity axis overlapping in nearby range cells, further diminishing the ability to resolve the scatterers.

From these results, it is clear that in order for TDMA to be feasible for range estimation, the waveform time T must be sufficiently large. The reduced unambiguous range for these results show all the scatterers from the scenario aliasing in range. Comparing unambiguous range spaces for the chosen operating parameters, the LFMCW-FDA emission clearly attains superior performance.

In summary, by compressing the virtual array into closely spaced delay bins, the LFMCW-FDA emission retains both unambiguous Doppler and range spaces, attaining superior performance over TDMA and DDMA in this manner. However, this also results in a diminished range resolution, and so both TDMA and DDMA attain superior range resolution. An adaptive algorithm is presented momentarily which aims to combat this loss in resolution.

3.7 Experimental Results

In July of 2022, an open-air data collection was performed to validate the simulated results of the LFMCW-FDA MISO system. The collection took place at Wright-Patterson Air Force Base, in conjunction with the Air Force Research Lab (AFRL) and Wright State University (WSU).

An RF System-on-Chip (SoC) was used as the transceiver. This setup along with the transmit and receive antennas are shown in the figures below.

Transmitter front end and antenna Receive Antenna

Figure 3.22: Transmit and receiver equipment

In the scene was a high RCS scatterer in the form of an all-terain vehicle with a top hat reflector strapped on the back. The transmit array and receive antenna were placed in a quasi-monostatic setup. The open-air scene along with representations of the scattering and radar platform geometry is shown in Figure 3.23, with the white dashed line representing the boresight direction of the transmit antenna.

Figure 3.23: Scene of open-air data collection

With the mobile top hat scatterer in the scene, several collections were performed, using the operating parameters summarized in the simulation section, from Table 3.1. The following results are from a particular collection where the top hat was moving inbound towards the radar platform at an angle off boresight.

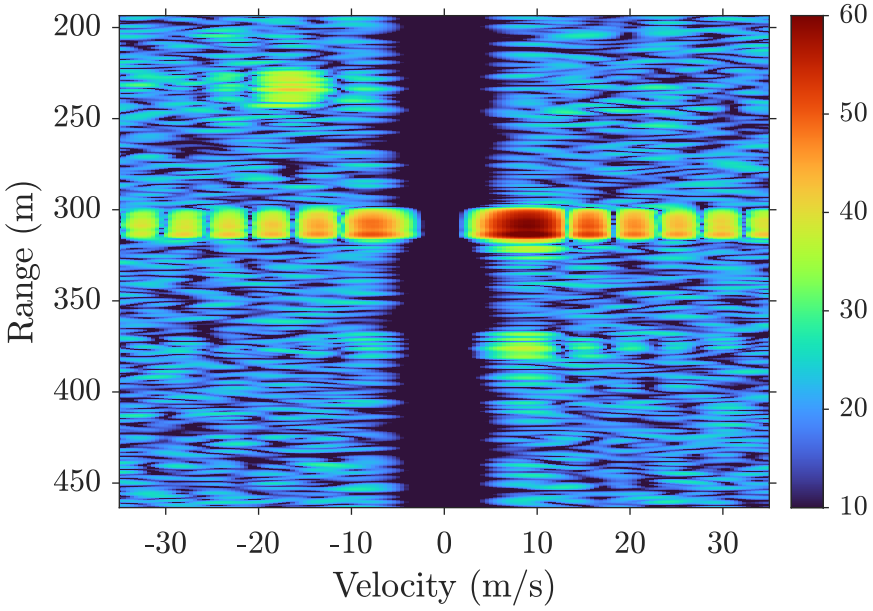

Figure 3.24: Range-velocity map, before spatial processing

In Figure 3.24, the range-velocity map is zoomed in slightly on the dominant scatterer in the scene, at roughly 314 m. The positive velocity shift shows a scatterer moving towards the radar

platform, which we can confidently assume is the tophat scatterer. There also does appear to be smaller responses from scatterers of opportunity in the area. These can be attributed to moving cars on the street farther off in range, outside of the unambiguous range space of 732 m, which have thus wrapped back into these range bins. Note that this response is oversampled for visual effect only.

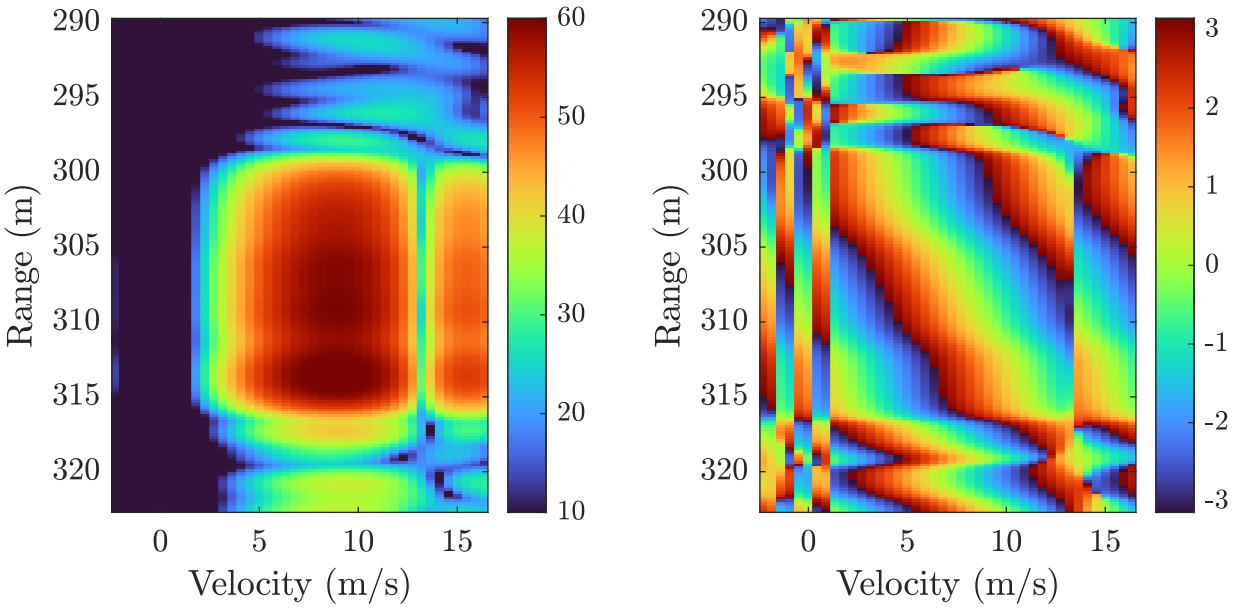

Figure 3.25: Zoomed in range-velocity map, magnitude (left) and phase angle (right)

Figure 3.25 shows the range-velocity map in both magnitude (right) and phase (left), zoomed in on the tophat scatterer response. The right image plots the instantaneous phase value at each range-Doppler bin, computed from the same range-Doppler data. Looking at the range-Doppler bins wherein the scattering response is located, a near linear phase progression can be observed across range. This is confirmation that the virtual array has formed along the delay dimension, as expected from the analysis and simulated results in the previous sections.

Forming the M virtual channels by circ-shifting the correlation response, a spatial angle estimate was made by beamforming the virtual channels at the range and velocity location with the largest response.

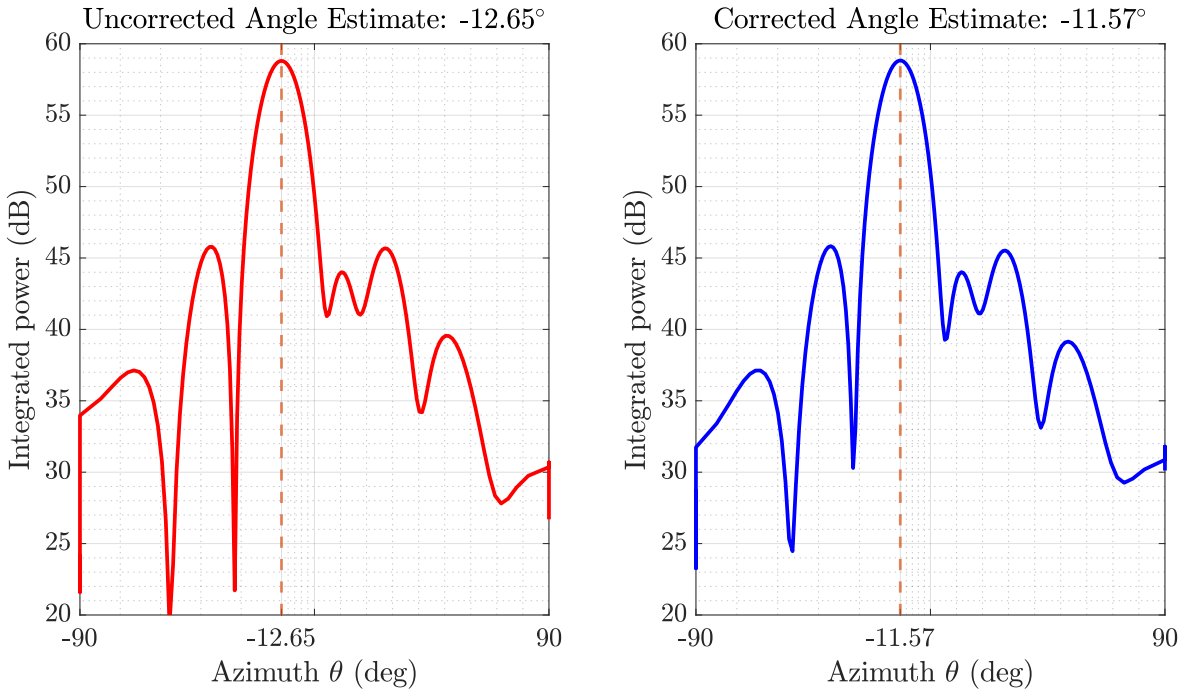

Figure 3.26: Beamforming response for scatterer, before and after video phase correction

The beamformer response to the left shows the estimate before video phase correction, and the response to the right shows the estimate after. To determine whether or not this difference before and after correction is reasonable, the video phase term was beamformed itself for this particular M, B & T.

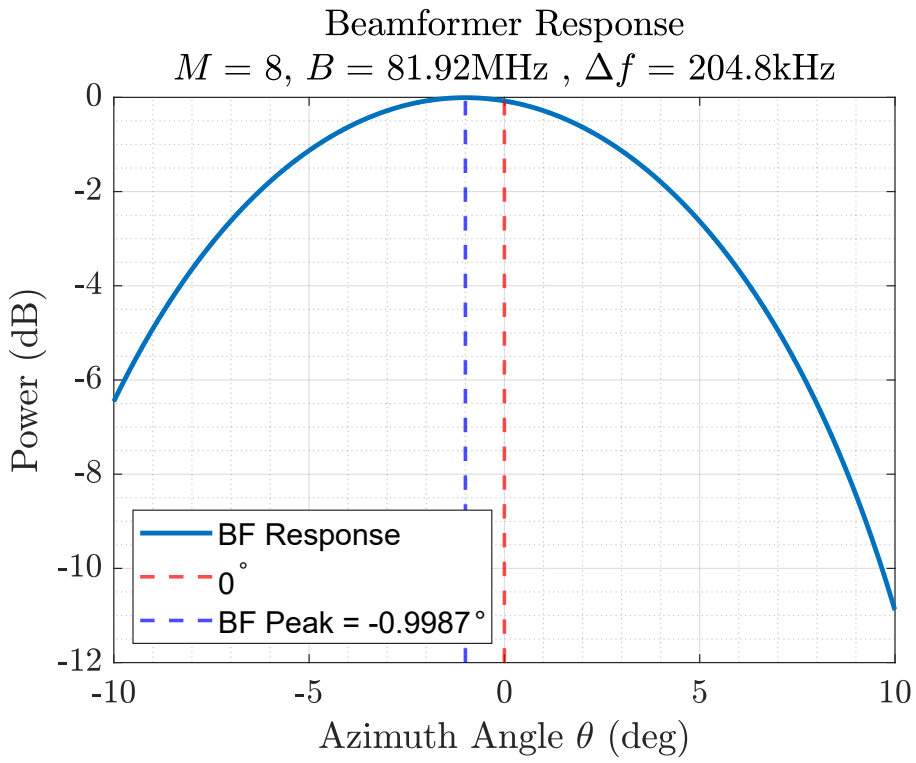

Figure 3.27: Expected video phase error

From Figure 3.27, what should be expected from this particular video phase error is about a $-1°$ deviation from the true spatial angle, which agrees with the before and after of Figure 3.26. With a clear peak in space, the post-beamforming range-velocity map is shown, evaluated for $\theta = -11.57°$

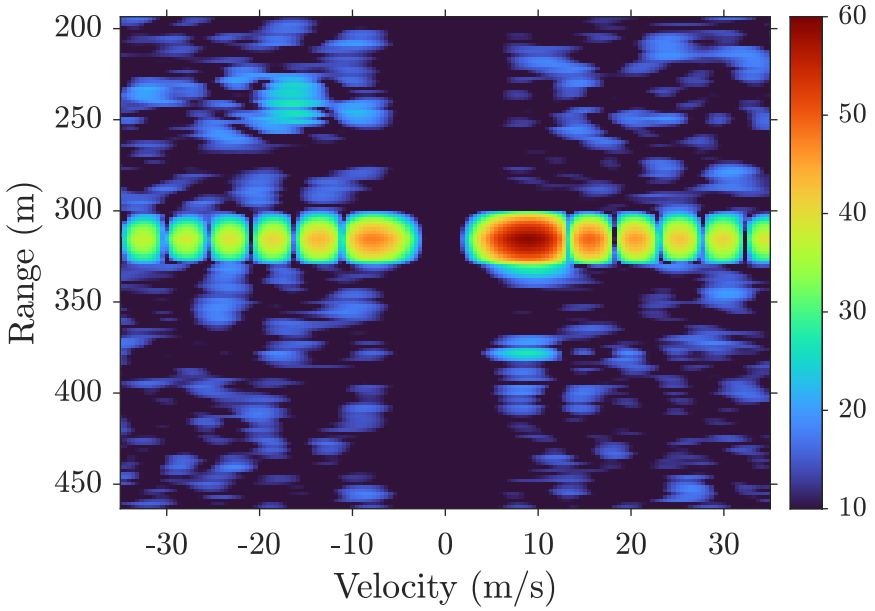

Figure 3.28: Range-velocity map, after spatial processing

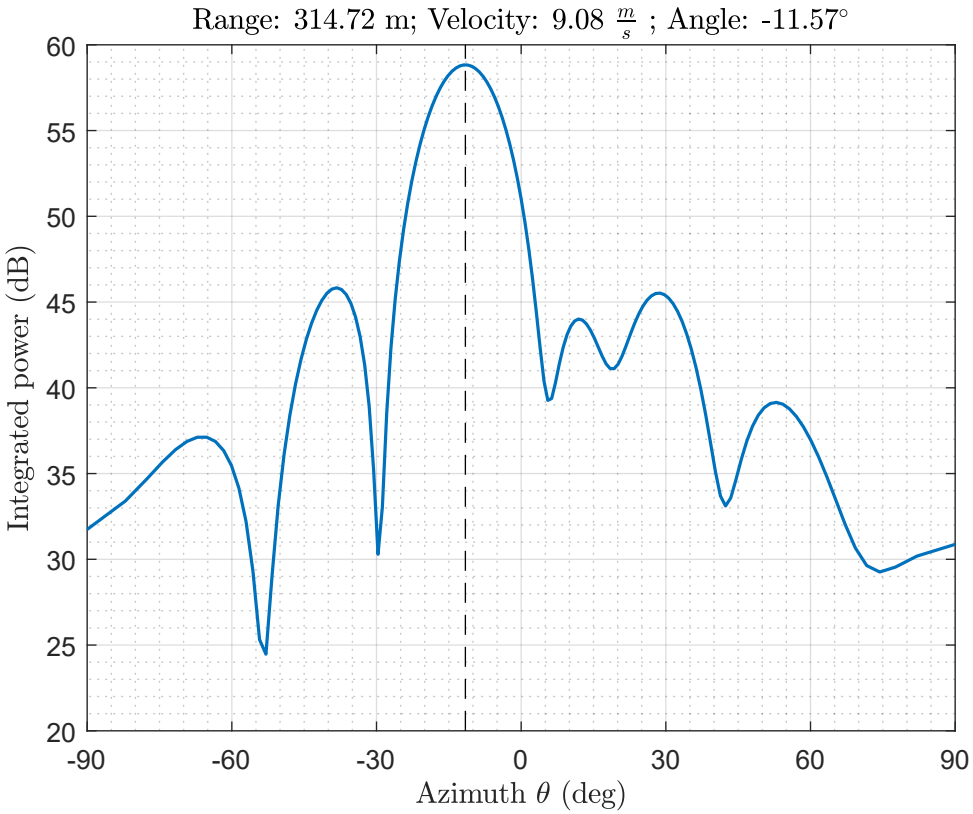

Figure 3.29: Final estimate of top-hat scatterer

Both Figures 3.28 and 3.29 are the final resulting data products, representing the range, velocity, and spatial estimates for the mobile top hat scatterer. Together, these experimentally validate the performance of the MISO LFMCW-FDA system. Additional open air data collections could be performed to capture more than one scatterer in the scene, particularly closely spaced in range and/or space, but the presented collection sufficiently validates the theory.

Chapter 4

Single Channel Adaptive Receive Processing

It was shown in the previous section that the range resolution for the LFMCW-FDA MISO system is degraded by the amount of transmit waveforms M. Due to the degraded range resolution, scatterers which are spaced close to each other in range can appear as one larger extended response, as opposed to two distinct responses. In this section, a modified version of the Single-Pulse Imaging (SPI) technique from [15] is introduced, which forms joint space-range filters, similar to the Space-Range Adaptive Processing (SRAP) approach as in [16]. Simulation results show the potential of the modified MISO LFMCW-FDA SPI algorithm to achieve a super resolution for closely spaced scatterers.

4.1 Single Pulse Imaging

The Single-Pulse Imaging (SPI) algorithm is based on the Reiterative Minimum Mean Square Error (RRMSE) [17] formulation first developed for Adaptive Pulse Compression (APC), where individual compression filters are adaptively formed for each delay bin. The filters are formed by nulling the responses from other scatterers so as to suppress sidelobe interference. First proposed in [18] with follow-up in [19], the SPI algorithm extends the adaptive nulling procedure to the fast-time Doppler dimension, i.e. over a single pulse.

Briefly introducing the algorithm as presented in [15], SPI assumes that for each Doppler frequency bin k, there exists a unique range profile $\mathbf{x}_k(l)$, illuminated by a unique waveform $\tilde{\mathbf{s}}_k$

$$\tilde{\mathbf{s}}_k = \mathbf{s} \odot \mathbf{p}_k$$

Where $\odot$ is the hadamard product, $\mathbf{s}$ is the discretized transmit waveform of length N and $\mathbf{p}_k$ is an N length Doppler phase progression vector for the θ_k Doppler shift, which can be expressed as:

$$\mathbf{p}_k = [1 \; e^{j\theta_k} ... e^{j\theta_k(N-1)}]^T$$

$$\theta_k = -\pi + \frac{2\pi}{K}(k-1), k = 1, ..., K$$

For receive sample index l, the receive signal can be modeled as a superposition of all K range profiles convolved with all Doppler shifted waveforms:

$$\mathbf{y}(l) = \sum_{k=1}^{K} \mathbf{S}_k \mathbf{x}_k(l) + \mathbf{v}(l) \tag{4.1}$$

Where $\mathbf{v}(l)$ is assumed additive noise of dimension Nx1, $\mathbf{S}_k$ is a convolution matrix of dimension Nx2N-1, and $\mathbf{x}_k(l)$ is a range profile vector of dimension 2N-1x1, with the following structures:

$$\mathbf{S}_k = \begin{bmatrix} \tilde{s}_k(N-1) & \tilde{s}_k(N-2) & \cdots & \tilde{s}_k(0) & 0 & \cdots & 0 \\ 0 & \tilde{s}_k(N-1) & \cdots & \tilde{s}_k(1) & \tilde{s}_k(0) & \cdots & 0 \\ \vdots & \vdots & \ddots & \vdots & \vdots & \ddots & \vdots \\ 0 & 0 & & \tilde{s}_k(N-1) & \tilde{s}_k(N-2) & \cdots & \tilde{s}_k(0) \end{bmatrix}$$

$$\mathbf{x}_k(l) = [x_k(l-N+1) ... x_k(l+N-1)]^T$$

The correlation filter $\mathbf{w}_k(l)$ is used to estimate scattering at delay l for the k^{th} Doppler profile:

$$\hat{x}_k(l) = \mathbf{w}_k^H(l)\mathbf{y}(l) \tag{4.2}$$

Non-adaptive estimates are generated from the familiar matched filter as

$$\mathbf{w}_k(l) = \frac{\tilde{\mathbf{s}}_k}{||\tilde{\mathbf{s}}_k||^2} \tag{4.3}$$

To mitigate the range sidelobes which mask closely spaced scatterers, adaptive RMMSE-based filters are constructed. The MMSE cost function is posed

$$J(l, \theta_k) = E[|x_k(l) - \mathbf{w}_k^H(l)\mathbf{y}(l)|^2]$$

Where $x_k(l)$ is the true scattering to be estimated, and $E[\cdot]$ is the expectation operator.

An initial scattering estimate is measured using (4.3), and from here, the adaptive filter is constructed for both k and l from

$$\mathbf{w}_{k,i}(l) = \hat{p}_{k,i}(l)(\mathbf{R}_{s,i} + \mathbf{R}_{z,i} + \mathbf{R}_v)^{-1}\tilde{\mathbf{s}}_k \tag{4.4}$$

for iteration index i. The $\mathbf{R}_{z,i}$ term is included to account for model mismatch, but for the purposes of proof of concept, this term is ignored. The power estimate for the current range-Doppler cell is

$$\hat{p}_{k,i}(l) = |\hat{x}_{k,i}(l)|^2$$

The structured signal covariance matrix is

$$\mathbf{R}_{s,i} = \sum_{k=1}^{K} \mathbf{S}_k \mathbf{P}_{k,i}(l)\mathbf{S}_k^H \tag{4.5}$$

The source covariance matrix (for scatterers assumed to be uncorrelated)

$$\mathbf{P}_{k,i} = [\hat{\mathbf{x}}_{k,i}(l)\hat{\mathbf{x}}_{k,i}^H(l)] \odot \mathbf{I} \tag{4.6}$$

Where $\mathbf{I}$ is an NxN identity matrix. Assuming white Gaussian noise with power σ_v^2, the noise correlation matrix

$$\mathbf{R}_v = E[\mathbf{v}(l)\mathbf{v}^H(l)] = \sigma_v^2\mathbf{I} \tag{4.7}$$

The algorithm in [15] is expanded further to include a beamspoiling for improved robustness. This will also not be included in these results, but could be included in future work to improve performance in a real system. For the purposes of this work, the formulations described above are sufficient to show the potential of the algorithm used in the MISO LFMCW-FDA system.

4.2 Modified SPI for LFMCW-FDA

The single pulse, Doppler discretized receive signal model of SPI proves itself readily feasible for modification to a discretized Spatial angle receive signal model. Using the analytic LFMCW-FDA correlation model from (A.17), the expected structure for a single point scatterer from the k^{th} spatial angle of arrival is used as the new signal model:

$$\hat{x}(\tau,\theta_k) = \gamma_o \sum_{m=0}^{M-1} e^{j\pi\sin(\theta_k)m} e^{j\frac{\pi}{T}m(\tau-\tau_o)} \left(1-\frac{|\tau-\tau_o|}{T}\right) sinc\left(\pi\left(m+B(\tau-\tau_o)\right)\left(1-\frac{|\tau-\tau_o|}{T}\right)\right) \tag{4.8}$$

Where θ_k is now treated as a spatial angle, as opposed to the Doppler shift phase progression from the previous section. Since this model already has the compressed responses isolated to delay bins uniformly distributed about the scattering delay τ_o, the dimensionality of the resulting discretized signal model vector can be reduced from signal length N to the length of the virtual array. In this work, the signal model used is the "critically" sampled case, where $fs = B$ and so the virtual array is of length M which is also the number of transmit antenna elements. For the discretized version of (4.8) $\mathbf{h}_k$, the modified SPI signal model is

$$\tilde{\mathbf{s}}_k = \mathbf{h}_k \tag{4.9}$$

Where $\mathbf{h}_k$ contains only the samples of the virtual array formed from the correlation response

to a scatterer arriving from the k^{th} spatial angle. $\tilde{\mathbf{s}}_k$ is now of dimension M, and the discrete index k spans the full set of K spatial angles, from $-90^\circ : 90^\circ$. Rewriting (4.1)

$$\mathbf{y}(l) = \sum_{k=1}^{K} \mathbf{H}_k \mathbf{x}_k(l) + \mathbf{v}(l) \tag{4.10}$$

Here $\mathbf{y}(l)$ now models the pulse compressed response signal for the k^{th} angle of arrival. $\mathbf{H}_k$ is a convolution matrix with the same structure as $\mathbf{S}_k$, with replacement of the waveforms with those defined in (4.9), and so is now of dimension Mx(2M-1). $\mathbf{x}_k(l)$ is likewise a reduced dimensionality range profile vector of dimension (2M-1)x1.

With this modification to the signal model, the SPI algorithm now adaptively forms range-space filters, with a reduced dimensionality which lowers the computation time required.

4.3 Simulation Results

To demonstrate the performance of the modified SPI algorithm for the LFMCW-FDA MISO system, the same waveform and system operating parameters were used as in the previous simulations, from Table 3.1 - except that only a single sweep was considered. The choice of 5 iterations of the modified SPI algorithm was chosen purely from observation of adequate performance.

First, a simulation was constructed where two scatterers where placed at the same delay bin, spaced a beamwidth apart from each other in space. The initial estimate $\hat{\mathbf{x}}_{k,0}(l)$ was formed using (4.3) for the signal model of (4.9), which is also the non-adaptive estimate.

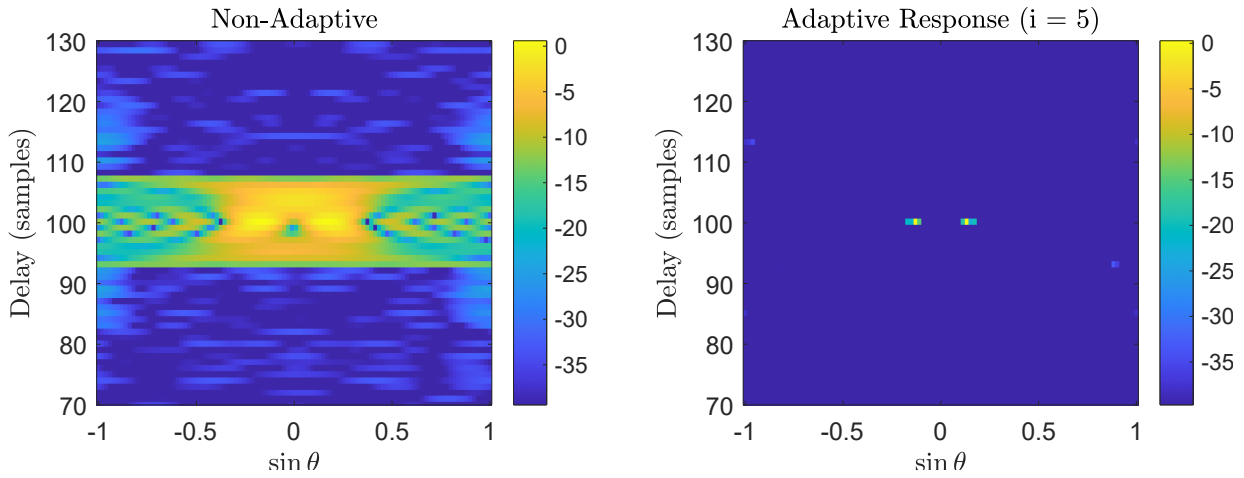

Figure 4.1: 2 scatterers at the same delay (true locations are red dots), beamwidth apart in spatial angle

The results from Figure 4.1 show a clear improvement in both space and range sidelobes, producing two distinct peaks near the true scattering locations.

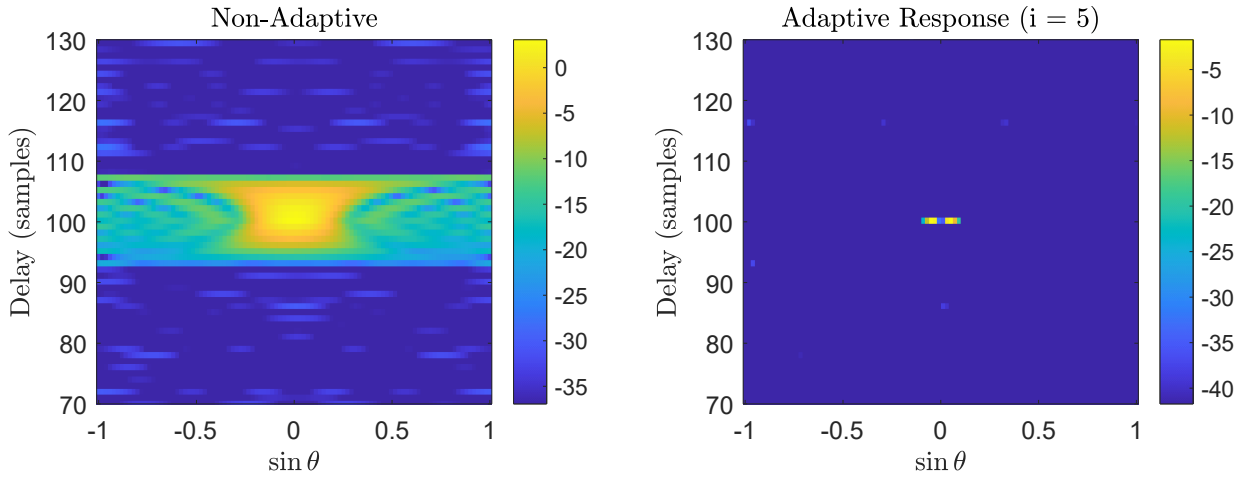

Figure 4.2: 2 scatterers at the same delay, half-beamwidth apart in spatial angle

To further show the capabilities of the modified SPI algorithm, the scatterers were moved closer in space, to half-beamwidth separation in space. The left subplot in Figure 4.2 shows the inability of the non-adaptive case to distinguish between the two - the response appears to be a single point scatterer. The right subplot meanwhile shows the adaptive response which once again clearly shows two distinct and separable peaks.

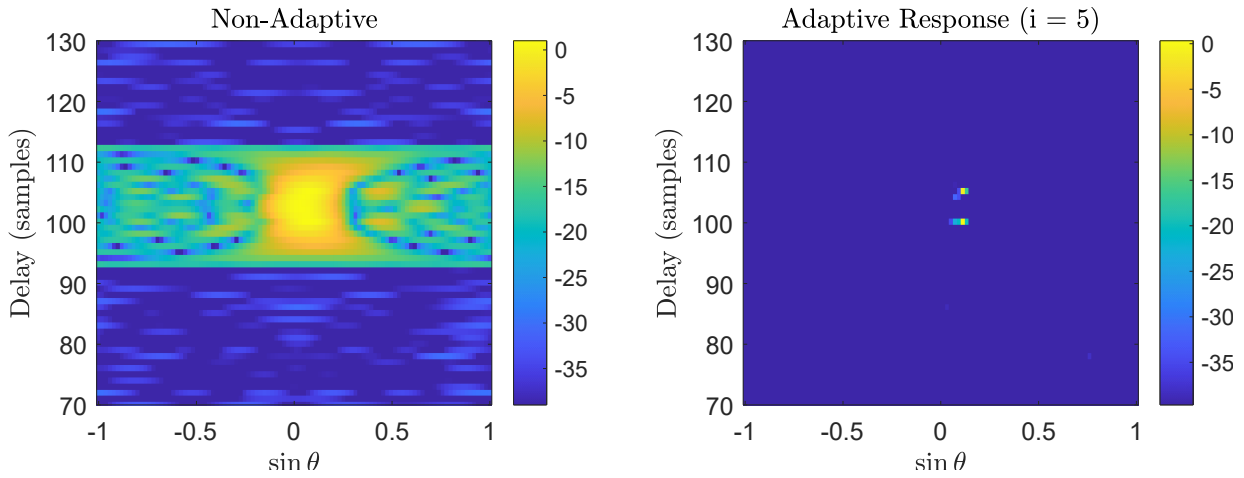

Figure 4.3: 2 scatterers at the same spatial angle, spaced 5 delay bins apart

Finally, two scatterers were placed at the same spatial angle, and spaced closely in delay, where the two virtual arrays overlap. Figure 4.3 shows the comparative responses, and demonstrates the capability to separate the two scatterers using the adaptive algorithm.

The results shown demonstrate the potential for the modified SPI algorithm to improve upon the performance of the MISO LFMCW-FDA system. Further analysis and potential modifications, such as addition of the model mismatch term and beamspoiling, are left for future work.

Chapter 5

Conclusion

The work in this thesis presented an implementation of a MISO LFMCW-FDA system. The system was shown to perform range, Doppler, and spatial estimation using a single receive antenna element, by taking advantage of the known spatially diverse transmission structure and the resulting virtual array formed along the delay dimension after correlation processing. An open-air data collection was performed where the expected performance was experimentally validated.

The MISO LFMCW-FDA emission structure and processing scheme was compared to two traditional spatially diverse MIMO structures: DDMA and TDMA. In DDMA, waveform separability is achieved along the Doppler dimension, at the expense of a reduced usable unambiguous Doppler space. In TDMA, waveform separability is achieved along the time dimension, at the expense of a reduced usable unambiguous range space. The proposed MISO LFMCW-FDA system achieves separability in the delay dimension with closely spaced responses, thus retaining the full unambigous range and Doppler spaces, at the expense of a reduced range resolution.

To combat the reduced range resolution, an adaptive correlation filter algorithm based on the SPI approach was introduced. The SPI algorithm was modified for spatial angle of arrival as opposed to fast-time Doppler. Using the analytical correlation model for the MISO LFMCW-FDA system as the signal model, filters with the length of the virtual array are formed, as opposed to full waveform length filters, reducing the overall dimensionality of covariance matrices being inverted, and thus reducing the required computation time. Simulation results show the ability to resolve scatterers with overlapping responses in both range and space. An open air data collection with multiple closely spaced scatterers would be needed to experimentally validate these results, but the preliminary simulation results show a promising adaptive technique to deal with the resolution

degradation in the delay dimension inherent to this system.

The potential of the FDA emission structure in a search radar context was examined, where the ability to increase the revisit rate for all spatial angles simultaneously introduces an attractive alternative to more traditional TWS or SAT approaches to search radar resource allocation. This coupled with the full unambiguous spaces and reduced range resolution implies the potential application as a low resolution search radar. The increased revisit rate comes with a reduced unambiguous range space however, and thus the ability to resolve ambiguous range returns is a source of potential future work.

An attractive feature of this system as a whole is the consequential low cost nature of the individual components. An LFMCW transmit array operates at a lower peak power than a pulsed system, reducing the need for costly front-end hardware. LFMCW system architectures are also generally not complex, and the frequency shifts for each element of the FDA can likewise be implemented in a straight forward manner. A single receive antenna directly results in less data handled, and the correlation processing presented in the non-adaptive receiver are made up of FFT's, which are likewise known to be computationally inexpensive. All of this together results in the potential of a real-time system implementable in hardware relatively inexpensively while achieving the performance demonstrated.

5.1 Future Work

Collected here is a summary of the key points of attack for future work and improvements to this system.

- Process open-air data collected with multiple moving scatterers present
- Extend the MISO LFMCW-FDA system to a 2-D transmit array
- Simulate and analyze the performance of a full search and track radar, comparing the LFMCW-FDA emission with the traditional scanning methods

- Compare the computational complexity of the adaptive processing algorithm to the non-adaptive processing scheme
- Experimentally validate the adaptive algorithm, to demonstrate the ability to improve separability of closely spaced scatterers in range and angle.
- Demonstrate the ability to resolve ambiguous returns in range and Doppler

References

[1] M. Skolnik. Attributes of the ubiquitous phased array radar. pages 101–106. Boston, MA, 2003.

[2] Dimitris G Manolakis. *Statistical and Adaptive Signal Processing : Spectral Estimation, Signal Modeling, Adaptive Filtering, and Array Processing*. Artech House, Boston, 2005.

[3] Jian Li and Petre Stoica. Mimo radar with colocated antennas. *IEEE Signal Processing Magazine*, 24(5):106–114, 2007.

[4] Wim van Rossum and Laura Anitori. Doppler ambiguity resolution using random slow-time code division multiple access mimo radar with sparse signal processing. In *2018 IEEE Radar Conference (RadarConf18)*, pages 0441–0446, 2018.

[5] Daniel J. Rabideau. Doppler-offset waveforms for mimo radar. In *2011 IEEE RadarCon (RADAR)*, pages 965–970, 2011.

[6] G. J. Frazer, Y. I. Abramovich, B. A. Johnson, and F. C. Robey. Recent results in mimo over-the-horizon radar. In *2008 IEEE Radar Conference*, pages 1–6, 2008.

[7] P. Antonik, M. C. Wicks, H. D. Griffiths, and C. J. Baker. Frequency diverse array radars. Verona, NY, 24 – 27 Apr. 2006.

[8] Arsen Turhaner, Simsek Demir, and Altunkan Hizal. Monopulse direction finding for linear frequency modulation based frequency diverse array. In *2017 IEEE Radar Conference (RadarConf)*, pages 0089–0094, 2017.

[9] Ramazan Çetiner, Çağrı Çetintepe, Şimşek Demir, and Altunkan Hizal. Prospects of FMCW-based frequency diverse array radar. *The Journal of Engineering*, 2019(21):7299–7303, 2019.

[10] P. Antonik, M.C. Wicks, H.D. Griffiths, and C.J. Baker. Multi-mission multi-mode waveform diversity. In *2006 IEEE Conference on Radar*, pages 3 pp.–, 2006.

[11] Aaron M. Jones and Brian D. Rigling. Planar frequency diverse array receiver architecture. In *2012 IEEE Radar Conference*, pages 0145–0150, 2012.

[12] Phillip E Pace. *Detecting and classifying low probability of intercept radar*. Artech House, Boston, 2004.

[13] Armin W Doerry. Coherent processing of up/down linear frequency modulated chirps. Technical Report SAND2020-12165, Sandia National Laboratories, 5301 Shawnee Rd, Alexandria, VA 22312, November 2020.

[14] Hongbo Sun, Frederic Brigui, and Marc Lesturgie. Analysis and comparison of MIMO radar waveforms. pages 1–6. Lille, France, 13–17 Oct. 2014.

[15] David G. Felton, Christian C. Jones, Daniel B. Herr, Lumumba A. Harnett, Shannon D. Blunt, and Christopher T. Allen. Experimental demonstration of single pulse imaging (spi). In *2023 IEEE Radar Conference*, 2023.

[16] Patrick M. McCormick, Thomas Higgins, Shannon D. Blunt, and Muralidhar Rangaswamy. Adaptive receive processing of spatially modulated physical radar emissions. *IEEE Journal of Selected Topics in Signal Processing*, 9(8):1415–1426, 2015.

[17] S. D. Blunt and K. Gerlach. Adaptive pulse compression via MMSE estimation. 42(2):572–584, Apr. 2006.

[18] S. D. Blunt, A. K. Shackelford, and K. Gerlach. Single pulse imaging. In *2006 International Waveform Diversity & Design Conference*, pages 1–5, 2006.

[19] Shannon D Blunt, Aaron K Shackelford, Karl Gerlach, and Kevin J Smith. Doppler compensation & single pulse imaging using adaptive pulse compression. 45(2):647–659, 2009.

[20] Mark A. Richards, James A. Scheer, and William A. Holm. *Principles of Modern Radar, Volume 1 - Basic Principles*. SciTech Publishing, 2010.

Appendix A

Analytic Representation of Correlation Response

This derivation assumes a single non-moving point scatterer (no Doppler), over a single sweep.

The unshifted transmit waveform $s(t)$ can be represented as:

$$s(t) = e^{j2\pi c_2(\frac{-B}{2}t + \frac{B}{2T}t^2)} \tag{A.1}$$

Where $c_2 = \pm 1$ denotes clock-wise/counter-clock-wise sweep.

The far-field radiated emission model $g(t,\theta)$ can be represented as:

$$g(t,\theta) = s(t)\sum_{m=0}^{M-1} e^{j2\pi m\frac{c_1}{T}t} e^{-j\pi c_1 m} e^{j\pi\sin(\theta)m} \tag{A.2}$$

Where $c_1 = \pm 1$ denotes an up/down chirp.

For a single point scatterer at delay τ_o, spatial angle θ_o, and complex scattering γ_o(and f_{D_o}= 0), the single channel receive signal $y(t)$ can be represented as:

$$\begin{aligned} y(t) &= \gamma_o g(t-\tau_o,\theta_o) \\ y(t) &= \gamma_o s(t-\tau_o)\sum_{m=0}^{M-1} e^{j2\pi c_1 m(t-\tau_o)/T} e^{-j\pi c_1 m} e^{j\pi\sin(\theta_o)m} \end{aligned} \tag{A.3}$$

The correlation response $\hat{x}(\tau)$ is represented as:

$$\begin{aligned}
\hat{x}(\tau) &= \frac{1}{T}\int_{-\infty}^{\infty} s^*(t-\tau)y(t)dt \\
\hat{x}(\tau) &= \frac{1}{T}\gamma_o \int_{-\infty}^{\infty} s^*(t-\tau)s(t-\tau_o)\sum_{m=0}^{M-1} e^{j2\pi c_1 m(t-\tau_o)/T} e^{-j\pi c_1 m} e^{j\pi \sin(\theta_o)m} dt \\
\hat{x}(\tau) &= \gamma_o \sum_{m=0}^{M-1} e^{-j\pi c_1 m} e^{j\pi \sin(\theta_o)m} \frac{1}{T}\int_{-\infty}^{\infty} s^*(t-\tau)s(t-\tau_o)e^{j2\pi c_1 m(t-\tau_o)/T} dt
\end{aligned} \tag{A.4}$$

Isolating the integral portion:

$$\frac{1}{T}\int_{-\infty}^{\infty} s^*(t-\tau)s(t-\tau_o)e^{j2\pi c_1 m(t-\tau_o)/T} dt \tag{A.5}$$

Performing a substitution of variables:

$$\begin{aligned}
\eta &= \tau - \tau_o \\
\bar{t} &= t - \tau_o \\
F &= \frac{c_1 m}{T}
\end{aligned} \tag{A.6}$$

Plugging this into the expression of (A.5):

$$\frac{1}{T}\int_{-\infty}^{\infty} s^*(\bar{t}-\eta)s(\bar{t})e^{j2\pi F\bar{t}} d\bar{t} \tag{A.7}$$

Notice that the expression (A.7) is in the form of the delay-Doppler ambiguity function $A(\tau, f_d)$ [20] for delay η and frequency F:

$$A(\eta, F) = \frac{1}{T}\int_{-\infty}^{\infty} s^*(\bar{t}-\eta)s(\bar{t})e^{j2\pi F\bar{t}} d\bar{t} \tag{A.8}$$

The ambiguity function form is useful in understanding intuitively why the correlation response takes the shape it does, as discussed in section 3.

Continuing the derivation, plug in (A.1) into (A.7) and expand:

$$\frac{1}{T}\int_{-\infty}^{\infty} e^{-j2\pi c_2[-\frac{B}{2}(\bar{t}-\eta)+\frac{B}{2T}(\bar{t}-\eta)^2]} e^{j2\pi c_2[-\frac{B}{2}\bar{t}+\frac{B}{2T}\bar{t}^2]} e^{j2\pi F\bar{t}} d\bar{t} \tag{A.9}$$

Rearranging and isolating terms which are dependent on $\bar{t}$ within the integral:

$$e^{-j2\pi c_2[\frac{B}{2}\eta+\frac{B}{2T}\eta^2]}\frac{1}{T}\int_{-\infty}^{\infty} e^{j\frac{2\pi}{T}[c_1 m+Bc_2\eta]\bar{t}} d\bar{t} \tag{A.10}$$

Due to the finite time-support over which a single sweep is defined [0:T], integration bounds differ for positive and negative delays τ.

For values of positive delays ($\tau \geq 0$) and setting aside the term outside the integral for now:

$$\frac{1}{T}\int_{\eta}^{T} e^{j\frac{2\pi}{T}[c_1 m+Bc_2\eta]\bar{t}} d\bar{t} \tag{A.11}$$

Evaluating the integral:

$$\frac{1}{T}\left(\frac{1}{j\frac{2\pi}{T}(c_1 m+Bc_2\eta)}\right)\left[e^{j\frac{2\pi}{T}(c_1 m+Bc_2\eta)T} - e^{j\frac{2\pi}{T}(c_1 m+Bc_2\eta)\eta}\right] \tag{A.12}$$

This expression can be rewritten as a scaled and phase rotated $sinc(\cdot)$ function. To do this, recall first

$$sinc(x) = \frac{\sin(x)}{x}$$

and from Euler's that

$$2j\sin(x) = [e^{jx} - e^{-jx}]$$

With this in mind, we can rewrite (A.12) as

$$\frac{1}{ja}[e^{ja} - e^{jb}]$$

Where

$$a = \frac{2\pi}{T}(c_1 m + Bc_2\eta)T$$

$$b = \frac{2\pi}{T}(c_1 m + Bc_2\eta)\eta$$

Now, we can multiply by $1 = \frac{e^{jc}}{e^{jc}}$ and rearrange terms in this manner:

$$\frac{1}{ja}\frac{e^{jc}}{e^{jc}}[e^{ja} - e^{jb}] = \frac{e^{-jc}}{ja}[e^{jd} - e^{-jd}] \tag{A.13}$$

Using Euler's identity as from above, rewrite this as:

$$\frac{e^{-jc}}{ja}[e^{jd} - e^{-jd}] = \frac{e^{-jc}}{ja} j2\sin(d)$$

Multiplying again by $1 = \frac{d}{d}$ and rearranging, now the expression can be written in the sinc form with the necessary phase and scaling:

$$\frac{e^{-jc}}{a}[sinc(d)]2d$$

Now to find c and d in terms of variables a and b, set up a linear system of equations using (A.13):

$$c + a = d$$

$$c + b = -d$$

Solving in terms of a and b:

$$c = -\frac{a+b}{2}$$

$$d = \frac{a-b}{2}$$

Plugging in a and b from above:

$$c = -\frac{\frac{2\pi}{T}(c_1 m + Bc_2\eta)(T+\eta)}{2}$$

$$d = \frac{\frac{2\pi}{T}(c_1 m + Bc_2\eta)(T-\eta)}{2}$$

Plugging in these values and simplifying, now (A.12) can be rewritten as:

$$e^{j\pi(c_1 m + Bc_2\eta)(1+\frac{\eta}{T})}(1-\frac{\eta}{T})sinc(\pi(c_1 m + Bc_2\eta)(1-\frac{\eta}{T})) \tag{A.14}$$

This results in (A.5) being rewritten as:

$$\frac{1}{T}\int_{-\infty}^{\infty} s^*(t-\tau)s(t-\tau_o)e^{j2\pi c_1 m(t-\tau_o)/T}dt = e^{-j2\pi c_2(\frac{B}{2}\eta+\frac{B}{2T}\eta^2)}e^{j\pi(c_1 m + Bc_2\eta)(1+\frac{\eta}{T})}(1-\frac{\eta}{T})sinc(\pi(c_1 m + Bc_2\eta)(1-\frac{\eta}{T})) \tag{A.15}$$

The complex exponential terms in front of the sinc can be simplified (recalling $\eta = \tau - \tau_o$):

$$e^{-j2\pi c_2(\frac{B}{2}\eta+\frac{B}{2T}\eta^2)}e^{j\pi(c_1 m + Bc_2\eta)(1+\frac{\eta}{T})} = e^{j\pi c_1 m}e^{j\frac{\pi}{T}c_1 m(\tau-\tau_o)}$$

And thus the whole correlation response (for $\tau > 0$) can be written as:

$$\hat{x}(\tau) = \gamma_o \sum_{m=0}^{M-1} e^{j\pi\sin(\theta_o)m}e^{j\frac{\pi}{T}c_1 m(\tau-\tau_o)}\left(1-\frac{\tau-\tau_o}{T}\right)sinc\left(\pi\left(c_1 m + Bc_2(\tau-\tau_o)\right)\left(1-\frac{\tau-\tau_o}{T}\right)\right) \tag{A.16}$$

By following the same process for $\tau < 0$, the resulting response for $|\tau|$ can be expressed as:

$$\hat{x}(\tau) = \gamma_o \sum_{m=0}^{M-1} e^{j\pi\sin(\theta_o)m}e^{j\frac{\pi}{T}c_1 m(\tau-\tau_o)}\left(1-\frac{|\tau-\tau_o|}{T}\right)sinc\left(\pi\left(c_1 m + Bc_2(\tau-\tau_o)\right)\left(1-\frac{|\tau-\tau_o|}{T}\right)\right) \tag{A.17}$$

Appendix B

Average Power Simplification Derivation

To reduce terms for compactness, the transmission at boresight ($\theta = 0°$) will be considered. The far-field signal transmitted in the boresight direction is thus (2.2) evaluated for $\theta = 0$:

$$g(t,0) = \frac{1}{M}\sum_{m=0}^{M-1} s(t)e^{j[2\pi\Delta Ft+\phi_0]m} \tag{B.1}$$

The average power of a signal transmitted in a particular spatial direction θ_i can be found by:

$$P = \frac{1}{T}\int_0^T |g(t,\theta_i)|^2\,dt \tag{B.2}$$

By plugging (B.1) into (B.2), using $|g(t)|^2 = g(t)\cdot g^*(t)$, and expanding the summation:

$$P_{FDA} = \frac{1}{TM^2}\int_0^T |s(t)|^2[1+e^{j[2\pi\Delta Ft+\phi_0]}+..+e^{j([2\pi\Delta Ft+\phi_0](M-1))}][1+e^{-j[2\pi\Delta Ft+\phi_0]}+..+e^{-j([2\pi\Delta Ft+\phi_0](M-1))}]\,dt$$

For compactness, choose $\alpha = 2\pi\Delta Ft+\phi_0$ so that

$$P_{FDA} = \frac{1}{TM^2}\int_0^T |s(t)|^2[1+e^{j\alpha}+..+e^{j\alpha(M-1))}][1+e^{-j\alpha}+..+e^{-j\alpha(M-1)}]\,dt$$

Isolating the product of complex exponential terms, multiple possible values for M can be plugged in and evaluated for, to find a pattern which can be described analytically. This process is as follows:

For $M = 2$:

$$[1+e^{j\alpha}][1+e^{-j\alpha}] = 2+2\cos(\alpha)$$

For $M = 3$:

$$[1 + e^{j\alpha} + e^{j2\alpha}][1 + e^{-j\alpha} + e^{-j2\alpha}] = 3 + 4\cos(\alpha) + 2\cos(2\alpha)$$

For $M = 4$:

$$[1 + e^{j\alpha} + e^{j2\alpha} + e^{j3\alpha}][1 + e^{-j\alpha} + e^{-j2\alpha} + e^{-j3\alpha}] = 4 + 6\cos(\alpha) + 4\cos(2\alpha) + 2\cos(3\alpha)$$

From these results, the pattern can be generalized for M elements as:

$$M + \sum_{m=2}^{M} 2(m-1)\cos(\alpha[M-m+1])$$

And thus

$$[1 + e^{j\alpha} + .. + e^{j\alpha(M-1))}][1 + e^{-j\alpha} + .. + e^{-j\alpha(M-1)}] = M + \sum_{m=2}^{M} 2(m-1)\cos(\alpha[M-m+1])$$

Appendix C

Calculation of Operating Parameters

For the following calculations, approximation of speed of light $c = 3x10^8$ m/s. Values for B, T, F_c, SRF, M, T_{CPI} taken from Table 3.1 in section 3.

$$\Delta R = M\frac{c}{2B} = (8)\frac{3x10^8}{2(81.92x10^6)} = 14.65 \text{ m}$$

$$R_{ua} = \frac{cT}{2} = \frac{(3x10^8)(4.8828x10^{-6})}{2} = 732 \text{ m}$$

$$\Delta v_d = \frac{\Delta f_d \lambda_c}{2} = \frac{\frac{1}{T_{CPI}} \cdot \frac{c}{F_c}}{2} = \frac{(\frac{1}{10x10^{-3}})(\frac{3x10^8}{3.3x10^9})}{2} = 4.55 \text{ m}$$

$$v_{r_{ua}} = \frac{f_{ua}\lambda_c}{2} = \frac{SRF\lambda_c}{2} = \frac{(204.8x10^3)(\frac{3x10^8}{3.3x10^9})}{2} = 9,309.1 \text{ m/s}$$